

Dynein-Driven Retrograde Intraflagellar Transport Is Triphasic in *C. elegans* Sensory Cilia

Highlights

- The *C. elegans* dynein-2 heavy chain undergoes triphasic retrograde IFT
- Ciliopathy-related mutations reduce transport speed and frequency of dynein-2
- Ciliary entry of dynein-2 requires its tail, light intermediate chain, and IFT-B
- IFT-43 and IFT-139 regulate dynein-2 motility in a partial redundant fashion

Authors

Peishan Yi, Wen-Jun Li,
Meng-Qiu Dong, Guangshuo Ou

Correspondence

guangshuoou@tsinghua.edu.cn

In Brief

Yi et al. find that dynein-2 undergoes triphasic retrograde IFT in *C. elegans* cilia. Ciliopathy-related mutations in dynein-2 reduce its transport speed and frequency. IFT-B, the dynein-2 tail, and light intermediate chain are essential for ciliary entry of dynein-2, and IFT-A subunits IFT-139 and IFT-43 redundantly regulate dynein-2 motility.

Dynein-Driven Retrograde Intraflagellar Transport Is Triphasic in *C. elegans* Sensory Cilia

Peishan Yi,¹ Wen-Jun Li,² Meng-Qiu Dong,² and Guangshuo Ou^{1,3,*}

¹Tsinghua-Peking Center for Life Sciences, School of Life Sciences and MOE Key Laboratory for Protein Science, Tsinghua University, Beijing 100084, China

²National Institute of Biological Science, 7 Science Park Road, ZGC Life Science Park, Beijing 102206, China

³Lead Contact

*Correspondence: guangshuoou@tsinghua.edu.cn

<http://dx.doi.org/10.1016/j.cub.2017.04.015>

SUMMARY

Cytoplasmic dynein-2 powers retrograde intraflagellar transport that is essential for cilium formation and maintenance. Inactivation of dynein-2 by mutations in *DYNC2H1* causes skeletal dysplasias, and it remains unclear how the dynein-2 heavy chain moves in cilia. Here, using the genome-editing technique to produce fluorescent dynein-2 heavy chain in *C. elegans*, we show by high-resolution live microscopy that dynein-2 moves in a surprising way along distinct ciliary domains. Dynein-2 shows triphasic movement in the retrograde direction: dynein-2 accelerates in the ciliary distal region and then moves at maximum velocity and finally decelerates adjacent to the base, which may represent a physical obstacle due to transition zone barriers. By knocking the conserved ciliopathy-related mutations into the *C. elegans* dynein-2 heavy chain, we find that these mutations reduce its transport speed and frequency. Disruption of the dynein-2 tail domain, light intermediate chain, or intraflagellar transport (IFT)-B complex abolishes dynein-2's ciliary localization, revealing their important roles in ciliary entry of dynein-2. Furthermore, our affinity purification and genetic analyses show that IFT-A subunits IFT-139 and IFT-43 function redundantly to promote dynein-2 motility. These results reveal the molecular regulation of dynein-2 movement in sensory cilia.

INTRODUCTION

Members of the dynein family are evolutionarily conserved molecular motors that utilize the energy of ATP hydrolysis to move toward the minus end of microtubules (MTs). Dyneins can be divided into the following three classes: axonemal dyneins, which drive the beating of flagellum and cilium; cytoplasmic dynein-1, which powers the intercellular transport of various cargos and helps the formation of mitotic spindles; and cytoplasmic dynein-2, which is employed in intraflagellar transport (IFT) along axonemal microtubules [1, 2]. Defects in dynein-based motility

are implicated in a number of disease processes, including primary ciliary dyskinesia, neurodegeneration, viral infection, and short rib-polydactyly syndromes (SRPSs) [3, 4]. The biochemical and biophysical mechanisms of dynein stepping along microtubules have been explored extensively, aided by the capability to produce engineered dynein motors. Equally essential is the ability to visualize how the dynein heavy chain moves in the cells of a living animal and to understand how disease-related mutations impair dynein motility; however, the enormous size of dynein (>500-kDa heavy-chain polypeptide) has hindered the genetic manipulation of this motor in metazoans.

Cilia play diverse roles in motility, sensory perception, and signaling. Human ciliopathies arise from ciliary defects and cause cystic kidney diseases, retinal degeneration, obesity, and various morphological abnormalities [5]. Ciliogenesis requires the IFT of ciliary precursors from the ciliary base to the distal tip, which are bound to macromolecular IFT particles that are composed of IFT-A and IFT-B protein subcomplexes [6]. Anterograde IFT is accomplished either by a single heterotrimeric kinesin-II or by the coordinate "handover" action of kinesin-II and homodimeric OSM-3-kinesin [7–10]. After cargo unloads at the ciliary tip, cytoplasmic dynein-2 performs retrograde IFT that recycles anterograde motors, IFT particles, and ciliary breakdown products back to the cell body [11–18]. Whole-genome sequencing studies have identified a large spectrum of mutations of cytoplasmic dynein-2 heavy chain (*DYNC2H1*) from patients with SRPSs and Jeune asphyxiating thoracic dystrophy (JATD), which are related to skeletal dysplasias characterized by short ribs, shortened tubular bones, polydactyly, and multisystem organ defects [3, 4, 19]. These mutations affect the highly conserved residues, ranging from the motor domain and linker region to the regulatory tail, and their effects on dynein-2 motility remain unexplored.

C. elegans affords an attractive system for studying dynein-2 in live metazoans. At the dendritic endings of sensory neurons, the axonemes emanate from the ciliary base and transition zone and consist of a middle segment built by 4-μm-long doublet microtubules from which nine singlet microtubules extend to construct the 2.5-μm-long distal segment [9, 20]. The dynein-2 holoenzyme of *C. elegans* is composed of the heavy chain (HC) CHE-3, the intermediate chain (IC) DYCI-1, the light intermediate chain (LIC) XBX-1, and the light chains (LCs) LC8, Tctex, and Roadblock [12–14]. Early studies of dynein-2-driven retrograde IFT in *C. elegans* revealed a unitary rate of retrograde IFT [9, 11, 13]. Two subsequent studies have used strains

expressing dynein-2 accessory subunits, notably XBX-1, to follow the dynamics of dynein-2 at significantly higher resolution than those previous studies [14, 21]. In the latter work, retrograde IFT was visualized with single-molecule sensitivity, revealing that the dynamic behavior of XBX-1 is complex, displaying previously undetected diffusive motion around the cilium base together with pauses and directional switches along cilia [21]. However, these studies are limited in the sense that they report the dynamics of dynein-2 accessory subunits, but these accessory subunit dynamics do not necessarily reflect the dynamics of the dynein-2 complex as a whole. For example, in our previous study, we observed that the majority of OSM-6/IFT52 and XBX-1 turned around at the distal tip of the cilium, whereas DYCI-1, DLC-1, and DYL-T-3 turned around at the middle and distal segments, plausibly reflecting changes in the composition of the accessory subunits that associate with the major IFT-dynein heavy-chain motor subunit as it moves from the tip to the base of the cilium [14]. In support of this notion, biochemical fractionation studies suggested that the interactions among dynein-2 subunits are probably weak [22, 23]. Such considerations led us to undertake the technically far more challenging approach of generating GFP knockin strains expressing endogenous levels of the fluorescently tagged dynein-2 heavy-chain subunit rather than tagging only an accessory subunit, which allows us to follow, for the first time, the dynamics of the motor subunit itself along cilia of living cells. Using this approach, we observed the previously undetected and surprising changes in rate of motility of the dynein-2 motor. By introducing pathogenic mutations of dynein-2 into the *C. elegans* genome, we show that the R295C mutation at the dynein tail alters this motor to move in a slow manner. We further find that IFT-139 and IFT-43 function redundantly to regulate dynein-2 motility. On the basis of these findings, we propose the molecular model for how dynein-2 movement is achieved in live cilia.

RESULTS

Triphasic Retrograde Movement of Dynein-2 Heavy Chain along the Ciliary Segments

To visualize IFT components at the endogenous expression level [24], we constructed knockin (KI) strains to label IFT motors and IFT particles with the different fluorophores (Figures 1A–1D). The single- or triple-fluorescence KI strains are indistinguishable from the wild-type (WT) nematodes in animal development, cilium length, or IFT speeds (Figures 1C–1E). Unlike the strains in which the fluorescent IFT components are overexpressed, the fluorescence from KI animals is fairly dim in the cell body and along the dendrite but is highly enriched in cilia (Figure S1A). Notably, kinesin-II (KLP-20::GFP) was restricted around the ciliary base and transition zone, whereas OSM-3-kinesin (OSM-3::GFP) was mostly distributed at the ciliary distal segments in KI animals (Figure 1F), which is consistent with the localization pattern observed using the single-copy GFP gene-insertion scheme [8].

In agreement with the early measurements using fluorescent dynein-2 accessory chains [13, 14], the GFP-tagged dynein-2 heavy chain in GFP::CHE-3 KI animals undergoes the antero-grade IFT at 0.7 $\mu\text{m/s}$ along the ciliary middle segments and at 1.2 $\mu\text{m/s}$ in the distal segments, which supports the view that

dynein-2 is delivered to the ciliary tip as the cargo of kinesin-II and OSM-3 kinesin. Previously, we observed IFT particles moving tip to base at unitary speeds of 1.1 $\mu\text{m/s}$, but with improved optics and the GFP KI reporter (Figures S1B and S1C; Movie S1), we now find that the dynein-2 heavy chain moves in the retrograde direction at two rates: first accelerating from 1.2 $\mu\text{m/s}$ to 1.5 $\mu\text{m/s}$ and then decelerating back to 1.2 $\mu\text{m/s}$ adjacent to the ciliary base (Figures 2A–2C and 2E; Movie S2). Mirroring the GFP::CHE-3 imaging, retrograde movement of IFT particles in the IFT-74::GFP KI animals also showed triphasic movement (Figures 2D and 2E; Movie S3).

Disease-Associated Mutations Affect Dynein-2 Motility

We reasoned that the essential residues in dynein-2 that regulate its retrograde movement might be present among existing dynein point mutations in patients. We selected four disease-related residues that are highly conserved in the dynein family (Figures 3A, S2A, and S2B). Two mutations from SRPS patients were located in the tail domain of dynein-2 heavy chain (DYNC2H1) [19], and another two mutations from patients with malformations in cortical development were located in the motor domain of dynein-1 heavy chain (DYNC1H1) [25]. The corresponding mutations in the *C. elegans* che-3 were R295C, R1384C, R1693C, and K2935Q (Figures 3A, 3B, and S2C). Based upon the structural insights of dynein family proteins [26, 27], R295 was predicted to be in the putative site for cargo docking or accessory subunit binding, R1384 was in the linker region between motor and tail domains that might participate in the power stroke, and R1693 and K2935 were located in the AAA1 and MT-binding domain (MTBD), respectively (Figures S3A–S3E). Using the MT-pelleting assay with recombinant MTBD proteins, we showed that the K2935Q mutation reduced the binding of MTBD to MTs by approximately 50% (Figures S3F–S3H).

To examine how these mutations affect dynein-2 motility, we knocked each mutation in the genome of the GFP::CHE-3 KI strain (Figure S2C). Although the animals carrying the R1384C mutation uptake the fluorescent lipophilic dye Dil from their sensory cilia as WT animals, the dye-filling efficiency was dramatically reduced in R295C animals and was completely abolished in R1693C and K2935Q animals. Consistently, the cilium length was marginally affected in R1384C animals, shortened in R295C and R1693C animals, and severely truncated in the K2935Q mutant animals (Figures 3C and 3D). We never observed retrograde IFT of dynein-2/CHE-3^{K2935Q}, in contrast to the robust transport that we consistently observed in WT worms (Figure 3E; Movie S4). Using MKSR-2::mCherry to mark the transition zone (Figures 2A and S4G), we observed accumulation of GFP::CHE-3^{K2935Q} and IFT52/OSM-6::mCherry in truncated cilia (Figures 3C and S4A), phenocopying che-3 null alleles, presumably because of their continuous anterograde transport but defective retrieval. Next, we measured IFT frequency and speed in dynein-2 carrying the R295C, R1384C, or R1693C mutation (Figures 3E–3I). In WT animals, we detected 0.6 or 0.4 IFT events of dynein-2 per second in the anterograde or retrograde direction, respectively; however, these mutations importantly reduced IFT frequencies in both directions (Figures 3E and 3I; Movie S4). Although the anterograde speeds of mutant dynein-2 (R295C and R1384C) do not show statistically significant variations from

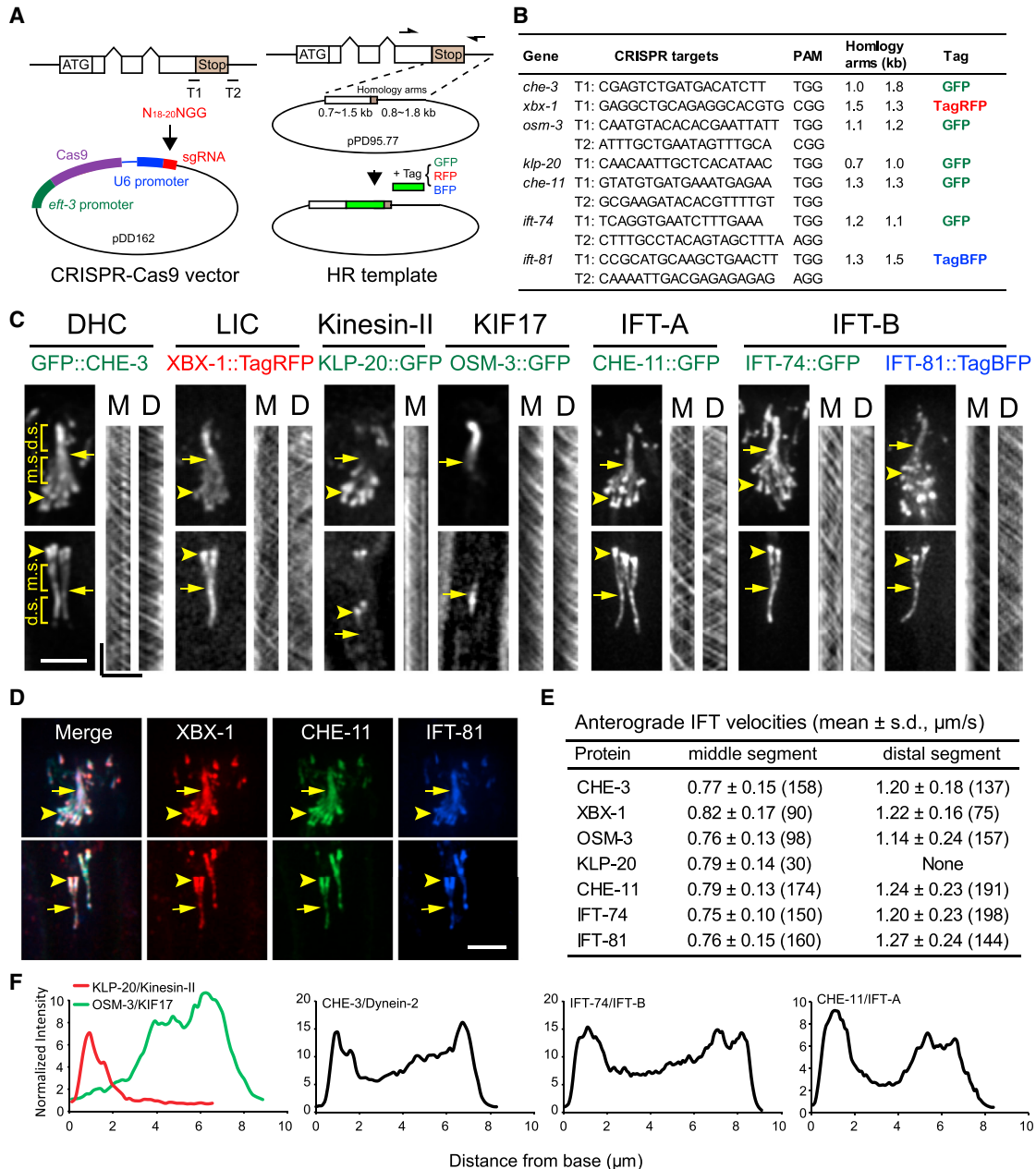


Figure 1. Generation of Knockin C. elegans Expressing Fluorescent IFT Components

(A) Schematic design of the CRISPR-Cas9-assisted knockin for *C. elegans*. One or two single-guide RNAs (sgRNAs) targeting the 5' or 3' ends of genes were added to pDD162 to generate the CRISPR-Cas9 plasmids (left), and ~1 kb homology arms and fluorescent tags were inserted into pPD95.77 to generate homology recombination (HR) templates (right). A pair of primers was designed to screen knockin progenies via PCR.

(B) Summary of CRISPR targets, homology arms, and tags used for IFT gene knockin. PAM, protospacer adjacent motif.

(C) Localization of the endogenously tagged IFT components in the amphid (top) and phasmid (bottom) cilia. Kymographs show particle movement along the middle (M or m.s.) or distal segments (D or d.s.). Arrowheads indicate ciliary base and transition zone, and arrows indicate junctions between the middle and distal segments. DHC, dynein-2 heavy chain; LIC, dynein-2 light intermediate chain. Images were taken at an exposure time of 200 ms. The scale bar represents 5 μm. The bars in kymographs represent (horizontal) 5 μm and (vertical) 5 s.

(D) Representative images show triple-fluorescence labeling of dynein-2 (XBX-1), IFT-A (CHE-11), and IFT-B (IFT-81) complexes. The scale bar represents 5 μm.

(E) Summary of anterograde velocities of IFT components at the middle and distal segments. Numbers of IFT particles are shown in the brackets.

(F) Representative intensity plots of IFT components along cilia. Intensities were all normalized to those at the dendrite endings.

See also Figure S1.

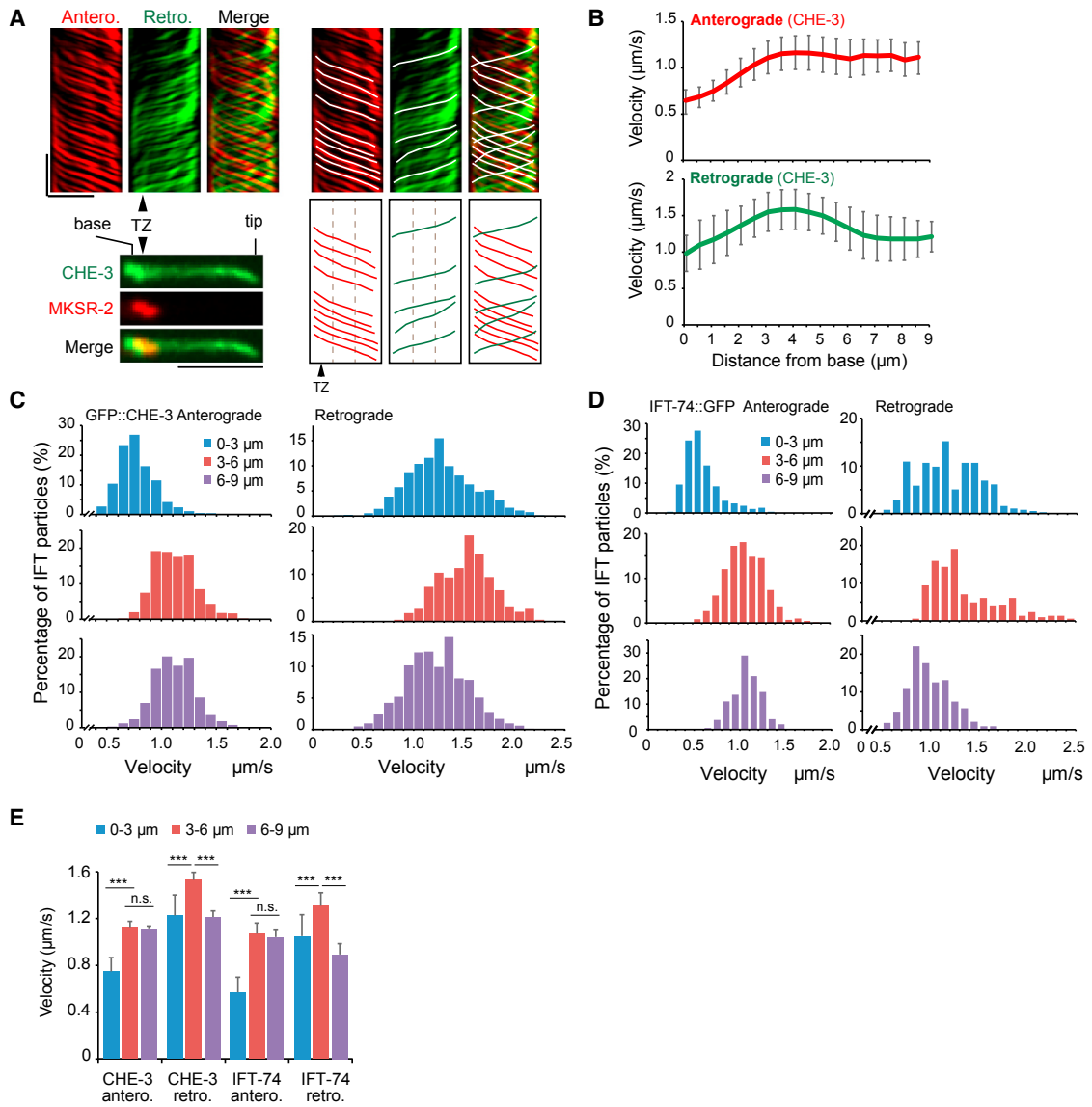


Figure 2. Dynein-2 and IFT-74 Movement in the Cilia of Knockin Animals

(A) Split kymographs show the anterograde (antero.) and retrograde (retro.) movement of GFP-tagged endogenous dynein-2 heavy chain CHE-3. Representative particle traces are marked with white lines. Arrowheads indicate transition zone (TZ) and its position in the kymographs. Cilium length was arbitrarily divided into three parts (dashed lines) for velocity quantification in (C)–(E): the ciliary base (0–3 μm), middle (3–6 μm), and tip (6–9 μm) regions. Images were taken at an exposure time of 100 ms. The scale bars represent 5 μm (horizontal) and 5 s (vertical).

(B) Quantification of GFP::CHE-3 anterograde (96 particles) and retrograde velocities (58 particles) along the cilia. See the STAR Methods for detailed method of velocity determination.

(C) Histograms of GFP::CHE-3 anterograde and retrograde velocity extracted from (B) at the ciliary base (blue), middle (red), and tip (purple) regions.

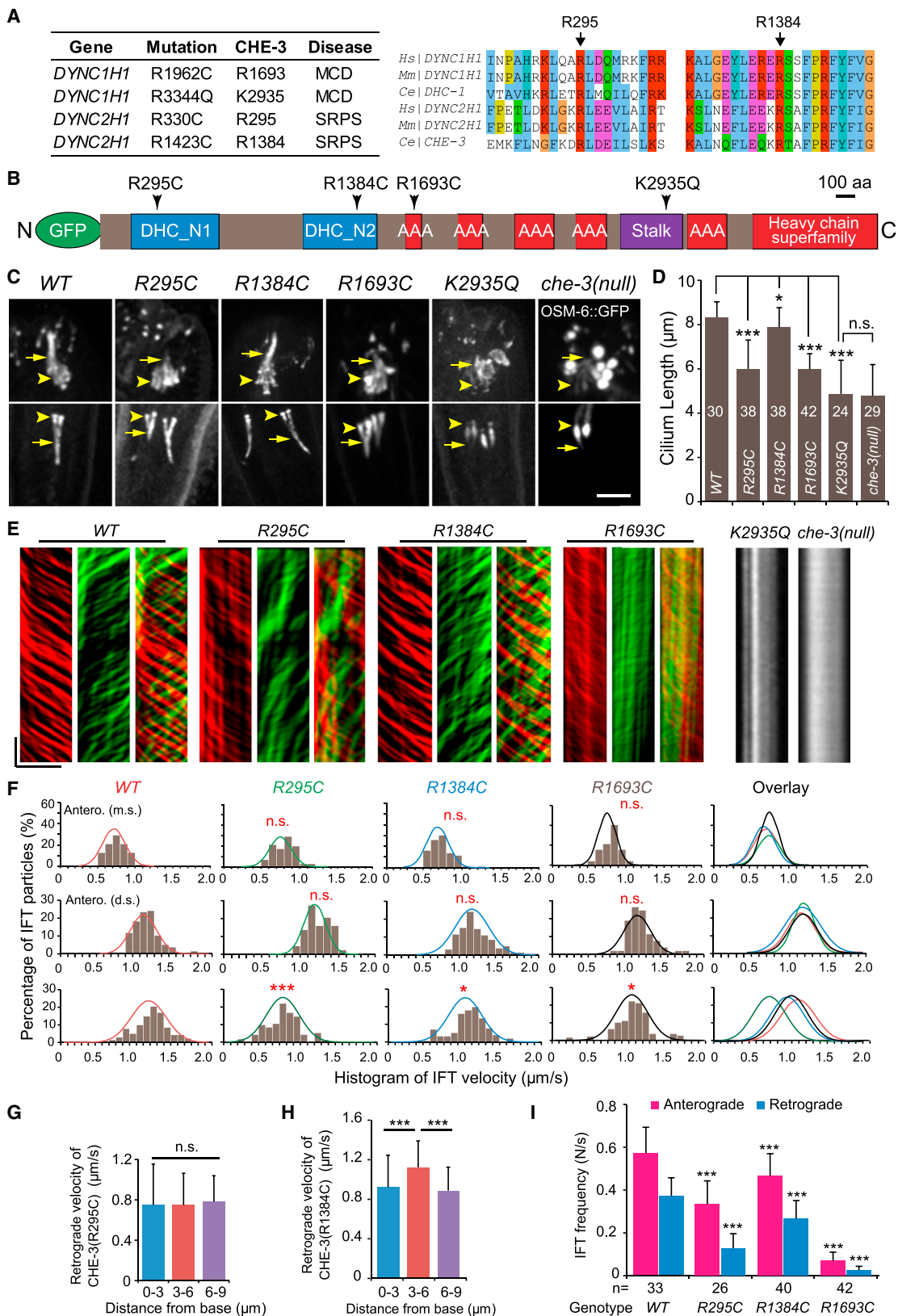
(D) Histograms of IFT-74::GFP anterograde (48 particles) and retrograde (18 particles) velocity at the ciliary base (blue), middle (red), and tip (purple) regions.

(E) Quantification of GFP::CHE-3 and IFT-74::GFP velocities (mean \pm SD) at the ciliary base, middle, and tip regions. “antero.” and “retro.” represent anterograde and retrograde transport, respectively. n.s., not significant; *** $p < 0.001$.

See also Figure S1 and Movies S1, S2, and S3.

those in WT cilia (Figure 3F), 24/121 IFT-particles (R295C; $n = 9$ animals) could not be tracked before reaching the ciliary tip (Figure 3E), and 12/167 particles (R1384C; $n = 11$ animals) changed their speeds in the distal segment (e.g., one acceleration, one deceleration, and two splitting into two traces in Figure 3E), which are consistent with the reduction of their cilium length and suggests that the defective kinesin-II and OSM-3 recycling may

reduce anterograde IFT frequency. In these *che-3* mutant alleles, multiple anterograde traces for dynein-2 appear interrupted in the ciliary middle segment when they encounter large retrograde trains (Figure 3E; 13/121 of GFP::CHE-3^{R295C} traces from nine animals, 10/167 of GFP::CHE-3^{R1384C} from 11 animals, and 9/55 of GFP::CHE-3^{R1693C} from eight animals). One possibility could be that dynein-2 loading on the anterograde IFT train



(legend on next page)

takes place normally, but their association is unstable such that dynein-2 falls off the train and returns to the base via its dynein activity. The overall retrograde IFT speed was mildly reduced by the R1693C mutation but severely impaired by R295C (Figure 3F). These results were further supported by our observations of fluorescent XBX-1, DYCI-1, and OSM-6 localization in dynein-2 mutant animals harboring the R295C or R1693C mutation (Figures S4B–S4J). Essentially, dynein-2^{R295C} moved at a constant and slow tip-to-base rate of 0.8 μm/s (Figure 3G), whereas the R1384C mutation affected its transport speed and frequency mildly (Figures 3F, 3H, and 3I). Together, our data indicated that these disease-associated mutations affect dynein-2 motility and that the R295C mutation in the dynein tail reduces IFT speed and frequency.

The Role of IFT-Train Subcomplex IFT-B in Ciliary Entry of Dynein-2

We characterized the additional 13 severe loss-of-function *gfp::che-3* mutant alleles (Figures 4A and 4B). These mutants showed strong defects in dye filling and developed short and bulged cilia similar to the *che-3*-null allele [11] (Figures 4C and S5A). We uncovered two distinct cellular localization patterns of the truncated GFP::CHE-3 proteins: the mutations in the tail domain completely abolished their ciliary localization, whereas the partial or complete deletion of the motor domain did not eliminate GFP fluorescence from the residual cilia (Figures 4B, 4C, and S5A–S5E). In an in-frame deletion allele (*cas527*) that removes a fragment in the linker region, the truncated GFP::CHE-3 was produced in the cell body but failed to localize to cilia. This observation suggests that the V828-L984 fragment may be involved in the ciliary localization of dynein-2 or that the truncated dynein-2 motor may be aggregated and stuck in the cell body (Figure 4C). Mutations in the dynein-2 light intermediate chain DYNC2LI1 also cause the SRPSs [28], and XBX-1::TagRFP or GFP::CHE-3 was no longer observed in the *che-3* or *xbx-1* mutant cilia, respectively (Figures 4C and S5C), which indicates their interdependence in ciliary localization and is consistent with the findings from mammalian cells, *C. reinhardtii* and *T. brucei* [16, 28–30]. These results show that the dynein-2 tail and acces-

sory chains, but not its motor domain, are required for the transport of dynein-2 from the cell body to cilia. Furthermore, the dynein-2 fluorescence accumulates in the residual cilia of *daf-10* or *che-11* mutants defective in IFT-A, whereas dynein-2 does not enter the remaining cilia of the IFT-B *osm-5/ift88* mutant animals, revealing an essential role of IFT-B in the ciliary entrance of dynein-2 (Figures 4D and 4E).

Identification of IFT Components from Knockin Animals by Mass Spectrometry

To identify ciliary regulators of dynein-2 activity, we performed GFP affinity purification and mass spectrometric analysis of GFP-tagged IFT components. We isolated three subunits in the kinesin-II holoenzyme from KAP-1::GFP transgenic animals and all the 14 known IFT-B components in *C. elegans* from IFT52/OSM-6::GFP strains with high specificity and abundance (Figures 5A and 5B). Furthermore, three kinesin-II subunits were identified from KLP-20::GFP knockin animals, and IFT-B components, with the exception of two peripheral subunits DYF-11/IFT54 and IFT-20, were isolated from IFT-74::GFP knockin strains (Figure 5B), demonstrating the feasibility of using GFP knockin animals and proteomic approaches to dissect IFT protein machinery in *C. elegans*.

Because IFT-A was involved in the regulation of retrograde IFT [6], we attempted to identify dynein-2 regulators through the purification of IFT-A-associated components. Previous biochemical studies showed that IFT-A was composed of IFT144, IFT140, IFT122, IFT139, IFT121, and IFT43 [31, 32]. Using CHE-11::GFP knockin strains, we obtained all of the known IFT-A components in *C. elegans*, including CHE-11/IFT140, DAF-10/IFT122, DYF-2/IFT144, and IFTA-1/IFT121 (Figure 5B). Importantly, we identified two unique targets, ZK328.7 and C25H3.12, with high abundance. By constructing translational GFP fusion reporters, we showed that ZK328.7a::GFP and C25H3.12::GFP are specifically expressed in the ciliated neurons and undergo IFT at the characteristic speeds as other IFT-particle components (Figures 5C–5F; Movie S5). ZK328.7 is a putative ortholog of IFT139 and was cloned as *ift-139* recently [33]. C25H3.12 shares a 14% and 13% identity to

Figure 3. Disease-Associated Mutations in the Dynein-2 Heavy Chain Impair Its Motility and Transport Frequency

- (A) Disease-associated mutations in dynein-1 and dynein-2 heavy chains and alignment of sequences flanking the two tail residues R295 and R1384 in CHE-3 (also see Figures S2A, S2B, and S3A–S3E). MCD, malformations in cortical development; SRPS, short rib-polydactyly syndrome.
- (B) Schematic domain structure of the GFP-tagged dynein-2 heavy chain CHE-3. Arrows indicate the four mutation sites. C, C terminus; N, N terminus. The scale bar represents 100 amino acids.
- (C) Amphiid (top) and plasmid (bottom) cilia morphology imaged with GFP-tagged wild-type (WT) or mutated CHE-3. Cilia in *che-3*(null) mutant were labeled with IFT52/OSM-6::GFP. Arrowheads indicate the ciliary base and transition zone. Arrows indicate the junctions between the middle and distal segments. The scale bar represents 5 μm.
- (D) Cilium length (mean ± SD) in WT and *che-3* mutant animals. Numbers of cilia used for quantification are shown in the bars. Cilium length was measured with WT or mutant GFP::CHE-3 fluorescence, which shows identical pattern as IFT particle marker IFT52/OSM-6::mCherry (Figure S4). Comparisons were performed between the WT and mutants or between K293Q and *che-3*(null). n.s., not significant; *p < 0.05; **p < 0.001.
- (E) Kymographs of GFP-tagged WT and mutated CHE-3. Green, retrograde IFT; red, anterograde IFT. Kymographs in the *che-3*(null) mutant were visualized with IFT52/OSM-6::GFP. Images were taken at an exposure time of 100 ms. The scale bars represent (horizontal) 5 μm and (vertical) 5 s.
- (F) Histogram of dynein-2 velocities. Top: anterograde IFT along the middle segments. Middle: anterograde IFT along the distal segments. Bottom: retrograde IFT. Each plot was fit by a Gaussian distribution. Comparisons were performed between the WT and mutants. n.s., not significant; *p < 0.05; **p < 0.001.
- (G) Retrograde velocities (mean ± SD) of GFP::CHE-3^{R295C} at the ciliary base, middle, and tip regions. n.s., not significant when any of the three compared with each other.
- (H) Retrograde velocities (mean ± SD) of GFP::CHE-3^{R1384C} at the ciliary base, middle, and tip regions. ***p < 0.001.
- (I) Anterograde (magenta) and retrograde (blue) IFT frequencies (mean ± SD) in the WT and CHE-3 mutant animals. Numbers of kymographs used for quantification are shown above the genotypes. Comparisons were performed between the WT and mutants. ***p < 0.001.

See also Figures S2–S4 and Movie S4.

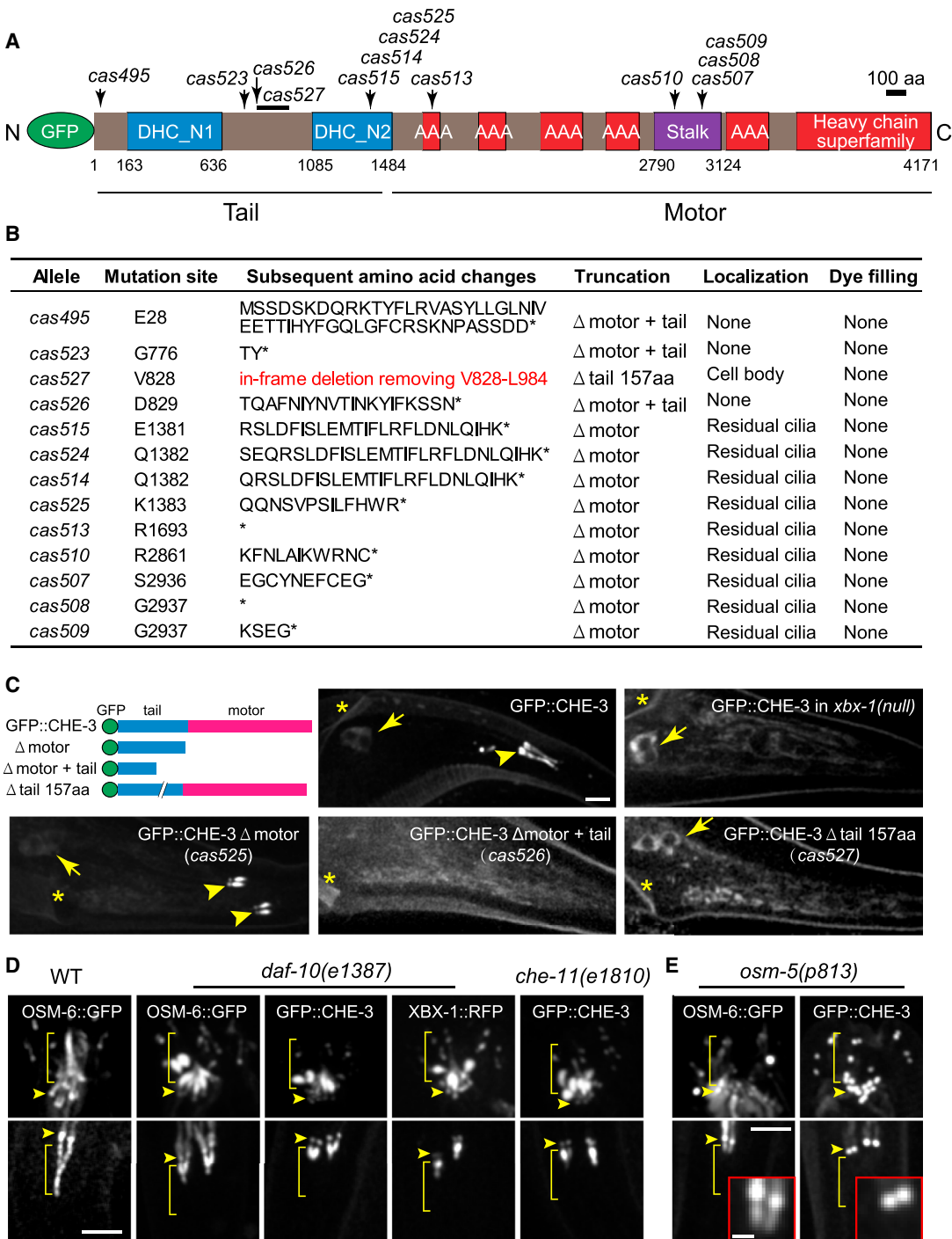


Figure 4. Ciliary Localization of Dynein-2 Requires Its Tail Domain, Light Intermediate Chain, and IFT-B, but not IFT-A

(A) Domain architecture of the GFP-tagged CHE-3. Arrows indicate various mutations introduced by CRISPR-Cas9.

(B) Mutation sites, amino acid changes, and resultant ciliary phenotypes of truncated GFP::CHE-3. All mutations cause frameshifts that introduce premature stop codons, except cas527, which is an in-frame deletion removing 157 amino acids between the DHC_N1 and DHC_N2 domains.

(C) Ciliary localization of WT and mutated GFP::CHE-3 in the phasmid neurons and cilia. Arrowheads indicate ciliary base. Arrows indicate cell body. Asterisks indicate anuses. The scale bar represents 5 μm.

(D) IFT-B component IFT-52/OSM-6::GFP and dynein-2 are localized to the residual cilia of IFT-A mutants (top, amphid; bottom, phasmid). The axonemal locations are indicated by square brackets (the same as below). The scale bar represents 5 μm.

(E) GFP::CHE-3 is absent from the ciliary compartments in the IFT-B mutant *osm-5(p813)*, whereas OSM-6::GFP is retained in the residual cilia. Phasmid cilia are enlarged in the red boxes. The scale bar represents 5 μm. The scale bar in the red box represents 1 μm.

See also Figure S5.

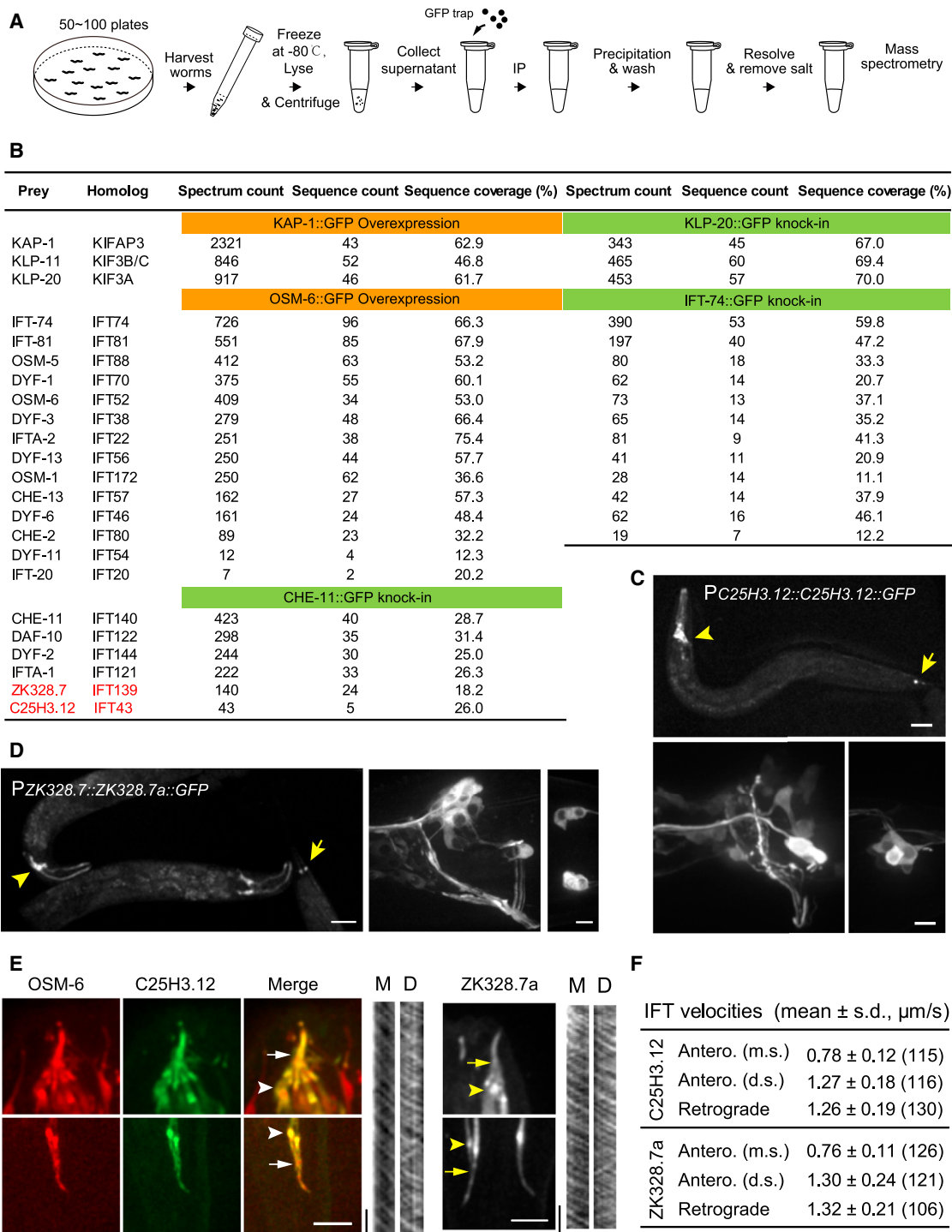


Figure 5. Identification of IFT-A Components IFT-139 and IFT-43 in *C. elegans*

- (A) Schematic workflow of GFP-based immunoprecipitation and sample preparation for mass spectrometry using transgenic or knockin worms.
- (B) Mass spectrometric results from the overexpression or knockin lines. Proteins that are homologs of subunits in kinesin-2, IFT-particle A, or IFT-particle B subcomplex were shown. ZK328.7 and C25H3.12 are putative IFT139 and IFT43 homologs, respectively.
- (C) Translational expression of C25H3.12::GFP in the head (arrowheads) and tail (arrows) neurons. The scale bars represent 50 μm (top) and 5 μm (bottom).
- (D) Translational expression of ZK328.7a::GFP in the head (arrowheads) and tail (arrows) neurons. The scale bars represent 50 μm (left) and 5 μm (right).
- (E) Localization of C25H3.12::GFP and ZK328.7a::GFP in the amphid (above) and phasmid (below) cilia. Kymographs show bidirectional movement along the ciliary middle (M) and distal (D) segments. Arrowheads indicate ciliary base and transition zone. Arrows indicate junctions between the middle and distal

(legend continued on next page)

human and *Chlamydomonas* IFT43 proteins, respectively (Figures S6A–S6C). We conducted GFP-affinity purification using the C25H3.12::GFP strains and identified IFT-A subunits, IFT-139, IFTA-1/IFT121, and DAF-10/IFT122 (Figure S6D), which suggests that C25H3.12 could be an IFT43 homolog, albeit of low sequence similarity. Hereafter, we refer to C25H3.12 as *ift-43*.

IFT-139 and IFT-43 Regulate Dynein-2 Motility

Mutations in human IFT139 ortholog *TTC21B* cause syndromic JATD and isolated nephronophthisis [34]. Whereas IFT particles accumulated at the ciliary tip of IFT139-deficient human or mouse cells, retrograde IFT was still evident and the mean retrograde speeds were reduced from 0.56 $\mu\text{m}/\text{s}$ to 0.41 $\mu\text{m}/\text{s}$ [35]. Consistent with the recent report [33], the *C. elegans* IFT components OSM-6::GFP, CHE-11::GFP, and IFT-74::GFP were accumulated in the ciliary distal segments of two putative null *ift-139* alleles (Figures 6A, 6B, and 6E; Movie S6). Although the loss of IFT-139 does not affect dynein-2 velocity or the ability of the animals to update Dil (Figures 6D and 6G; Movie S6), the retrograde transport frequency of dynein-2 was markedly reduced and GFP::CHE-3 occasionally forms aggregates at the distal tip of *ift-139* mutant cilia (Figures 6D and 6F). These mild ciliary phenotypes indicate that IFT-139 is involved in retrograde IFT but also suggest that other components may function together with IFT-139 to regulate dynein-2 in a partial redundant manner.

Human IFT43 homolog is mutated in Sensenbrenner syndrome, a heterogeneous ciliopathy that is characterized by skeletal anomalies [36, 37]. Whereas IFT-B components accumulate at the ciliary tip in the patient fibroblasts, no statistically significant difference in cilium length was detected between patient and control cells [36]. Intriguingly, mutations of IFT43 in *Chlamydomonas* caused the short flagella [38]; the different ciliary phenotypes may be resulted from the low sequence similarity among IFT43 homologs. We generated three large deletion alleles of the *C. elegans* *ift-43* that are severely truncated, lacking most of its coding sequence (Figure 6A). In agreement with the normal cilium length in patient cells, *ift-43* mutant animals exhibit no defects in their cilium length, IFT, or the dye-filling assay (Figures 6B, 6C, and 6G; Movie S6).

Whereas IFT-43 and IFT-139 possibly play minor roles in ciliogenesis, functional redundancy may be involved. In the single mutants, the fluorescence of OSM-6::GFP extended the same 8- μm distance from the ciliary base as in WT animals, suggesting that, in the absence of IFT-43 or IFT-139 function, IFT particles are transported normally all along the axoneme (Figure 6C). The cilium length and IFT in the single *ift-43* or *ift-139* mutant animals are distinct from those observed in other IFT-A mutant cilia; for example, the average length of *dyf-2* mutant cilia was reduced to 2.8 μm and OSM-6::GFP accumulated in the residual cilia [39]. However, in multiple independent *ift-43*; *ift-139* double mutant strains, the ciliary phenotypes are identical to those in the dynein-2 or IFT-A-null mutants: no fluorescent dye could be filled

into ciliated neurons and IFT particles accumulated along the residual 5- μm -long cilia (Figures 6B–6G and S6E; Movie S7), indicating that IFT ceases and IFT particles are not moved away from the shortened cilia. Indeed, in *ift-43* or *ift-139* single-mutant cilia, dynein-2 moves along both middle and distal segments at the characteristic rates as those in WT cilia, whereas no dynein-2 motility was observed in *ift-43*; *ift-139* double mutant cilia (Figures 6D and 6G), indicating that IFT-43 and IFT-139 function redundantly to regulate dynein-2 motility. Considering that IFT particles are more severely accumulated than dynein-2 in *ift-139* mutant cilia (Figures 6B, 6D, and 6E), we propose that IFT-43 and IFT-139 may regulate dynein-2 activity by docking the motor to its cargo, such as IFT-A, in a partial redundant mode.

Next, we performed a bimolecular fluorescence complementation (BiFC) assay to examine the spatial proximity between IFT-43/IFT-139 and XBX-1 [40]. IFT-43 and IFT-139 showed fluorescence complementation with XBX-1 (Figures 7A and 7B), indicative of the close proximity between IFT-A complex and dynein-2. In contrast, no fluorescence complementation was observed from the BiFC pair of KLP-20 and OSM-3, which is consistent with the view that kinesin-II and OSM-3 may be associated with the IFT-A and IFT-B complexes, respectively (Figure 7C) [7]. The close proximity between IFT-43/IFT-139 and XBX-1 individually may explain the functional redundancy of two IFT-A subunits in the regulation of dynein-2 motility (Figure 7D).

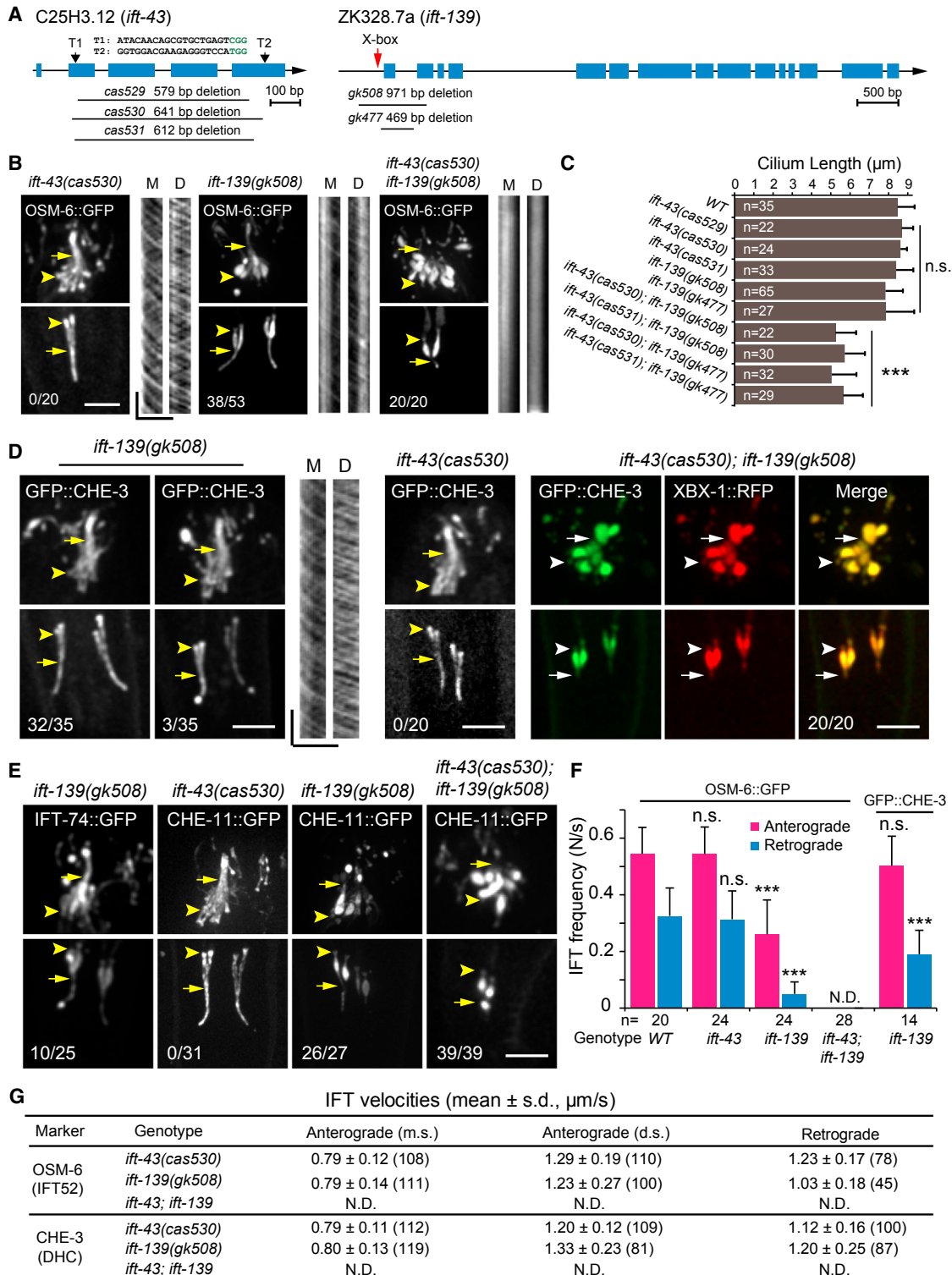
DISCUSSION

This study has introduced advanced genetic, imaging, and biochemical techniques to study dynein-2 motility *in vivo*. The combination of GFP-knockin and high-resolution live microscopy has allowed us to, for the first time, observe the triphasic retrograde movement of dynein-2 along distinct ciliary domains. We show that ciliary entry of dynein-2 requires IFT-B and that the dynein-2 tail and IFT-A subunits IFT-43 and IFT-139 regulate dynein-2 motility. We propose a molecular model for how dynein-2 behaves in the *C. elegans* ciliated neurons. Dynein-2 may be delivered as the cargo molecule by other motor proteins along the dendrites to the ciliary base, as the dendritic transport of dynein-2 does not require its motor domain but depends on its tail (Figures 4B and 4C). At the ciliary base, dynein-2 is proposed to be transported as a cargo, bound to IFT particles, by kinesin-2 motors to the ciliary tip (Figure 7E). At the ciliary tip, dynein-2 may be activated by cargo molecules likely through the interactions mediated by IFT-43 and IFT-139 (Figures 7D and 7E). These results reveal the regulatory mechanism of dynein-2 movement and provide insights into dynein-2-associated ciliopathies.

This study demonstrates that dynein-2 undergoes multiple phases of movement, which is in contrast to a unitary tip-to-base velocity described in the early studies [8, 9, 13, 14, 21]. One distinct feature of the previously overexpressed IFT markers is that there is a high level of background fluorescence instead of

segments. Images were taken at an exposure time of 200 ms. The scale bar in images represents 5 μm . The bars in kymographs represent 5 μm (horizontal) and 5 s (vertical).

(F) Summary of anterograde (antero.) and retrograde velocities C25H3.12 and ZK328.7a. m.s., middle segment; d.s., distal segments.
See also Figure S6 and Movie S5.

**Figure 6. IFT-139 and IFT-43 Function Redundantly to Regulate Retrograde IFT**

(A) Genomic structures of *ift-43* and *ift-139*. Three deletions of *ift-43* were generated by CRISPR-Cas9 knockout with two targets on the second (T1) and last (T2) exons. The red arrow indicates an X-box motif at the proximal promoter region of *ift-139*. Two deletions removing the X-box motif and N-terminal region are indicated.

(B) Cilium morphology in *ift-43* and *ift-139* single and double mutants. Kymographs show OSM-6/IFT52 movement at the middle (M) and distal (D) segments. Images were taken at an exposure time of 200 ms, and numbers of worms with particle accumulation in cilia are indicated at the bottom (the same as below).

(legend continued on next page)

clear retrograde traces from the knockin strains. In *Chlamydomonas*, anterograde and retrograde IFT both occur at unitary rates [41]; however, anterograde IFT in *C. elegans* sensory cilia uses two kinesin-2 motors to produce biphasic motility, whereas retrograde IFT uses dynein-2 yet occurs in a triphasic fashion. The biphasic anterograde IFT is achieved by the concerted action of two kinesin motors of the same polarity moving toward the same direction [9], whereas the triphasic retrograde IFT is generated by dynein-2 with the modulation of different accessory subunits and cargo molecules. Considering that the full assembly of the dynein-2 holoenzyme may be a time-consuming process, the slow retrograde IFT of the partially assembled dynein-2 could be advantageous for preventing the accumulation of anterograde kinesins and IFT trains at the ciliary tip. Multiphasic movement of motor proteins may reflect the fine coordination of intracellular transport by regulators and cargo molecules.

The transition zone has been proposed to be an obstacle for kinesin-2 motility in both anterograde and retrograde directions [8], and the deceleration of dynein-2 may represent physical obstacle due to transition zone barriers. Using double fluorescence labeling [42], we found that the transition zone protein MRSR-2::mCherry localizes in the region where the running GFP::CHE-3 particles reduce their speeds (Figure 2A), which suggests that the transition zone may function as the physical hindrance for dynein-2 in retrograde IFT. Lissencephaly 1 is generally considered to act as a molecular “clutch” that suppresses dynein motility and causes it to form a tight binding complex with the MT tracks [2]. The *C. elegans* LIS-1 is restricted within the ciliary middle segment adjacent to the transition zone [14] and may participate locally in active dynein-2 to decelerate the motor. Cytoplasmic dynein-1 has been shown to act as a gear in response to load [43]; the high load of dynein-2 at the ciliary base may contribute to the deceleration phase. Kinesin-II is likely to be inactivated by DYF-5/mitogen activated protein (MAP) kinase-mediated phosphorylation [44]; post-translational modifications of dynein-2 could also modulate the motor velocity. The change of dynein-2 speed can be caused by other factors, such as the local ciliary environment or the presence of doublet or singlet microtubules, whose number can be variable in *C. elegans* [20].

The constant slow velocity of dynein-2^{R295C} suggests that dynein-2 motility is regulated by the dynein tail, to which dynein accessory subunits bind. In agreement with the notion that the dynein tail coordinates the motor activity, the *Loa* mutation (F580Y) within the dynein-1 tail of mutant mice inhibits motor

run length by perturbing motor domain coordination [45]. Dynein-1 speed and processivity require accessory subunits, such as BiCD2 and the dynactin complex [46]. Likewise, the purified human dynein-2 heavy chain only moves at 70 nm/s in microtubule gliding assays [22]; however, retrograde IFT occurs at 0.5 $\mu\text{m}/\text{s}$ in mouse renal cilia, 1.3 $\mu\text{m}/\text{s}$ in *C. elegans* sensory cilia, 3.5 $\mu\text{m}/\text{s}$ in *Chlamydomonas* flagella, and 5.6 $\mu\text{m}/\text{s}$ in *Trypanosoma* flagella [35, 41, 47]. The apparent discrepancy may reflect the different resources of dynein-2 but also suggests that accessory subunits or the putative cargo adaptors promote dynein-2 motility. Our early work showed that several dynein-2 accessory subunits undergo turnaround at a distance away from the ciliary tip [14], raising the possibility that dynein-2 accessory subunits may be gradually associated with the heavy chain and speed it up along the axonemal middle segment (Figure 7E). Both anterograde and retrograde frequencies of TagRFP-marked XB-1 were twice lower than those of GFP::CHE-3 (Figure S4D). Similarly, anterograde and retrograde frequencies of OSM-6::mCherry are also twice less than those of OSM-6::GFP (Figure S4K), challenging the use of red fluorescent proteins along with GFP in double-fluorescent motility assays. The dynein-2 composition is heterogeneous across the cilium length that was arbitrarily divided into three parts (Figure 2A) [14], and it is possible that the dynein-2 composition is also heterogeneous among different trains within the same ciliary segments or that IFT components are not always associated.

The previous studies indicate that the duration times of a complete IFT cycle are similar in *Trypanosome*, *Chlamydomonas*, *C. elegans*, and mammalian LLC-PK1 cells (10–13 s), despite the different cilium length and IFT rates [47]. Our data support the notion that the IFT speeds are faster in the longer cilia: the *C. elegans* dynein-2 moves at 1.3 $\mu\text{m}/\text{s}$ in average for 7.5 μm in the retrograde direction, whereas the retrograde IFT reaches 5.6 $\mu\text{m}/\text{s}$ for 22.3 μm in *Trypanosoma*. The brightness of retrograde IFT particles is generally dimmer than anterograde ones (Figure 2A) [47–49]. In *Trypanosoma*, the anterograde IFT particles split into multiple small particles, causing the higher retrograde frequency [47]. In *C. elegans*, the frequency of retrograde transport for XB-1 dynein component is 1.6-fold higher than that of anterograde [21], which may also contribute to the balance of anterograde and retrograde IFT. The lower frequency from the knockin animals is presumably because of different systems used for expression and/or imaging. The previous single-molecule imaging showed that OSM-3-kinesin undergoes turnaround immediately [8]; however, the incoming IFT material spends 3 or 4 s at the ciliary

Arrowheads indicate the ciliary base and transition zone. Arrows indicate junctions between the middle and distal segments. The scale bar in images represents 5 μm . The bars in kymographs represent 5 μm (horizontal) and 5 s (vertical).

(C) Cilium length (mean \pm SD) in *ift-43* and *ift-139* single and double mutants. Numbers of cilia used for quantification are shown in the bars. Comparisons were performed between the WT and mutants. n.s., not significant. ***p < 0.001.

(D) Dynein-2 localization and movement in *ift-139* and *ift-43* single and double mutants. The accumulation of GFP::CHE-3 was only occasionally found in *ift-139* single mutant. The scale bar in images represents 5 μm . The bars in kymographs represent 5 μm (horizontal) and 5 s (vertical).

(E) Endogenously labeled IFT particles (IFT-74/IFT-B and CHE-11/IFT-A) accumulate in *ift-139* single mutant and *ift-43*; *ift-139* double mutant, but not in *ift-43* single mutant. The scale bar represents 5 μm .

(F) Anterograde (magenta) and retrograde (blue) IFT frequencies (mean \pm SD) in *ift-139* and *ift-43* single and double mutants. Numbers of kymographs used for quantification are shown above the genotypes. Comparison was performed between WT and mutants. N.D., not detectable. n.s., not significant. ***p < 0.001.

(G) IFT velocities of OSM-6/IFT52 and CHE-3/DHC in *ift-139* and *ift-43* single and double mutants. Numbers of cilia used for quantification are shown in the brackets. N.D., not detectable.

See also Movies S6 and S7.

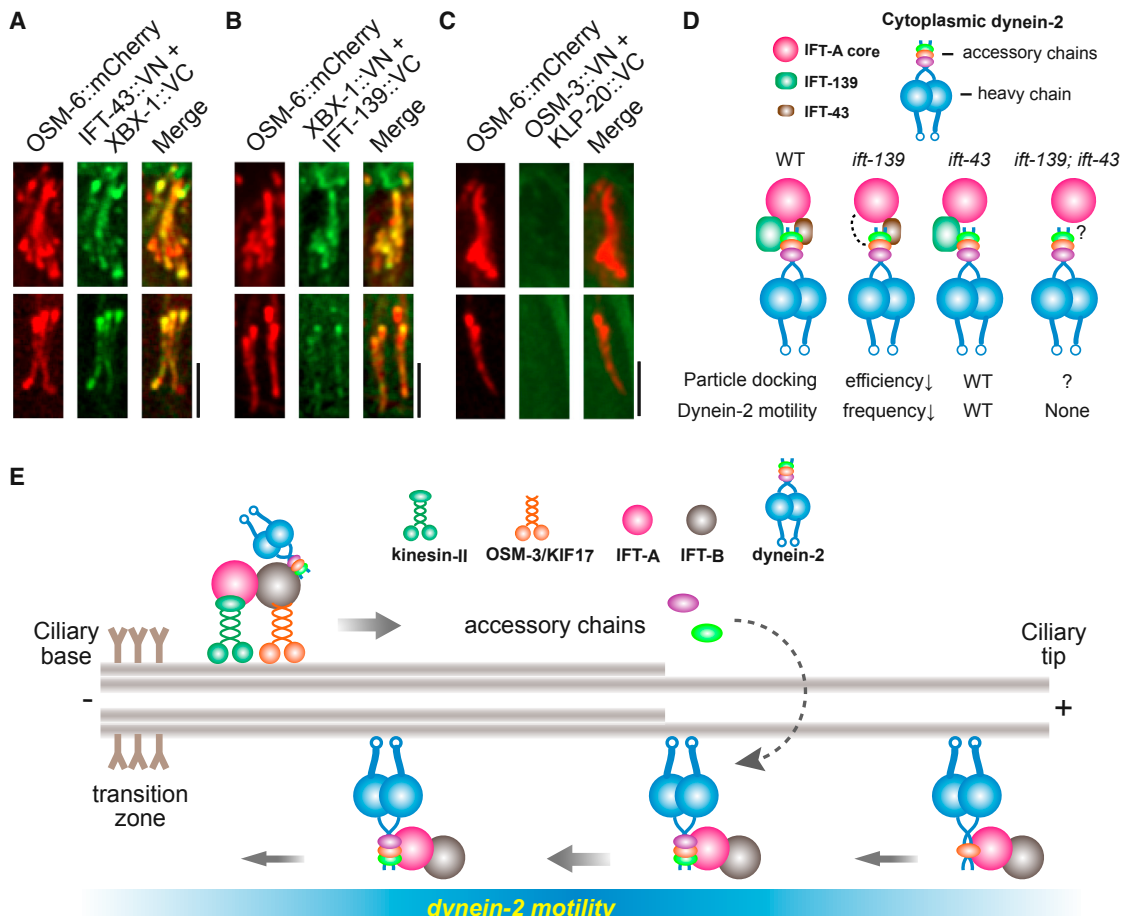


Figure 7. In Vivo Proximity between IFT-A and Dynein-2 and a Working Model Illustrating Dynein-2 Movement in Cilia

(A) The bimolecular fluorescence complementation (BiFC) assay shows that IFT-43 and XBX-1 approximate each other in vivo, indicating a possible interaction between them. The N-terminal fragment (VN) or C-terminal (VC) fragment of Venus was fused to IFT-43 or XBX-1, respectively. The scale bar represents 5 μm.

(B) BiFC assay shows that IFT-139 and XBX-1 approximate each other in vivo.

(C) OSM-3 and KLP-20 do not show fluorescence complementation in the BiFC assay.

(D) A model illustrating the redundant roles of IFT-139 and IFT-43 in regulating dynein-2 motility. Loss of *ift-139* alone causes reduction of retrograde frequency and accumulation of IFT particles but does not affect dynein-2 velocity. Although movement of dynein-2 and IFT particles is completely wild-type in *ift-43* single mutant, dynein-2-driven retrograde IFT is severely blocked in *ift-43; ift-139* double mutant.

(E) A model of dynein-2 dynamics in cilia. Dynein-2 is transported to the ciliary tip by kinesin-2 as a cargo. This process requires dynein-2 heavy-chain tail, light intermediate chain, and IFT-B. Upon recycling, IFT-139 and IFT-43 may activate dynein-2 by docking IFT particles onto this motor. The regulation of dynein-2 motility may also involve the incorporation of dynein-2 accessory chains and hindrance of transition zone.

tip before returning to the base in *Trypanosome* [47], and the *C. elegans* dynein-2 or IFT components may also undergo a transition phase at the ciliary tip.

The recent advances in sequencing technology have enabled the discovery of more than 50 causal loci of human ciliary diseases [50]. As hundreds of genes are crucial for ciliary structure and function, additional ciliopathy-related mutations will be identified. However, without functional annotation, sequencing data alone are not sufficient to establish the causal relationship or to offer appropriate resolution for understanding diseases. This study demonstrates the advantage of using a genetic model organism to investigate the basic mechanisms of pathogenic mutations. Our strategy facilitates the phenotypic analysis of disease-associated mutations in knockin animals, requiring only 3 weeks beginning from the experimental design in *C. elegans*.

STAR★METHODS

Detailed methods are provided in the online version of this paper and include the following:

- **KEY RESOURCES TABLE**
- **CONTACT FOR REAGENT AND RESOURCE SHARING**
- **EXPERIMENTAL MODEL AND SUBJECT DETAILS**
- **METHOD DETAILS**
 - Molecular biology
 - Genome editing
 - Microinjection and transgenesis
 - Dye-filling assay
 - Live cell imaging
 - Image processing and analysis

- Mass spectrometry
- Structure analysis, bioinformatics and biochemistry
- QUANTIFICATION AND STATISTICAL ANALYSIS

SUPPLEMENTAL INFORMATION

Supplemental Information includes six figures, one table, and seven movies and can be found with this article online at <http://dx.doi.org/10.1016/j.cub.2017.04.015>.

AUTHOR CONTRIBUTIONS

G.O. and P.Y. conceived this project. P.Y. performed the experiments and collected and analyzed the data under the supervision of G.O. G.O. and P.Y. wrote the manuscript. W.-J.L. and M.-Q.D. provided guidance on mass spectrometry.

ACKNOWLEDGMENTS

We thank Drs. R. Vale, A. Carter, J. Scholey, A. Roberts, T. Schroer, A. Leschziner, and J. Raff for discussions regarding this project; Caenorhabditis Genetics Center (CGC) for providing some strains; and the Protein Chemistry Facility at the Center for Biomedical Analysis of Tsinghua University for sample analysis. This work was supported by the National Basic Research Program of China (973 Program; grants 2013CB945602 and 2012CB945002), the National Natural Science Foundation of China (grants 31171295, 31190063, 31222035, 31301134, 31525015, and 31561130153), and the Newton Advanced Fellowship (grant NA140490) from the Royal Society.

Received: February 2, 2017

Revised: March 24, 2017

Accepted: April 10, 2017

Published: May 4, 2017

REFERENCES

1. Roberts, A.J., Kon, T., Knight, P.J., Sutoh, K., and Burgess, S.A. (2013). Functions and mechanics of dynein motor proteins. *Nat. Rev. Mol. Cell Biol.* **14**, 713–726.
2. Cianfrocco, M.A., De Santis, M.E., Leschziner, A.E., and Reck-Peterson, S.L. (2015). Mechanism and regulation of cytoplasmic dynein. *Annu. Rev. Cell Dev. Biol.* **31**, 83–108.
3. Merrill, A.E., Merriman, B., Farrington-Rock, C., Camacho, N., Sebald, E.T., Funari, V.A., Schibler, M.J., Firestein, M.H., Cohn, Z.A., Priore, M.A., et al. (2009). Ciliary abnormalities due to defects in the retrograde transport protein DYNC2H1 in short-rib polydactyly syndrome. *Am. J. Hum. Genet.* **84**, 542–549.
4. Dagoneau, N., Goulet, M., Geneviève, D., Sznajer, Y., Martinovic, J., Smithson, S., Huber, C., Baujat, G., Flori, E., Tecco, L., et al. (2009). DYNC2H1 mutations cause asphyxiating thoracic dystrophy and short rib-polydactyly syndrome, type III. *Am. J. Hum. Genet.* **84**, 706–711.
5. Ishikawa, H., and Marshall, W.F. (2011). Ciliogenesis: building the cell's antenna. *Nat. Rev. Mol. Cell Biol.* **12**, 222–234.
6. Taschner, M., and Lorentzen, E. (2016). The intraflagellar transport machinery. *Cold Spring Harb. Perspect. Biol.* **8**, a028092.
7. Scholey, J.M. (2013). Kinesin-2: a family of heterotrimeric and homodimeric motors with diverse intracellular transport functions. *Annu. Rev. Cell Dev. Biol.* **29**, 443–469.
8. Prevo, B., Mangeol, P., Oswald, F., Scholey, J.M., and Peterman, E.J. (2015). Functional differentiation of cooperating kinesin-2 motors orchestrates cargo import and transport in *C. elegans* cilia. *Nat. Cell Biol.* **17**, 1536–1545.
9. Snow, J.J., Ou, G., Gunnarson, A.L., Walker, M.R., Zhou, H.M., Brust-Mascher, I., and Scholey, J.M. (2004). Two anterograde intraflagellar transport motors cooperate to build sensory cilia on *C. elegans* neurons. *Nat. Cell Biol.* **6**, 1109–1113.
10. Cole, D.G., Diener, D.R., Himelblau, A.L., Beech, P.L., Fuster, J.C., and Rosenbaum, J.L. (1998). *Chlamydomonas* kinesin-II-dependent intraflagellar transport (IFT): IFT particles contain proteins required for ciliary assembly in *Caenorhabditis elegans* sensory neurons. *J. Cell Biol.* **141**, 993–1008.
11. Signor, D., Wedaman, K.P., Orozco, J.T., Dwyer, N.D., Bargmann, C.I., Rose, L.S., and Scholey, J.M. (1999). Role of a class DHC1b dynein in retrograde transport of IFT motors and IFT raft particles along cilia, but not dendrites, in chemosensory neurons of living *Caenorhabditis elegans*. *J. Cell Biol.* **147**, 519–530.
12. Schafer, J.C., Haycraft, C.J., Thomas, J.H., Yoder, B.K., and Swoboda, P. (2003). XB-1 encodes a dynein light intermediate chain required for retrograde intraflagellar transport and cilia assembly in *Caenorhabditis elegans*. *Mol. Biol. Cell* **14**, 2057–2070.
13. Hao, L., Efimenko, E., Swoboda, P., and Scholey, J.M. (2011). The retrograde IFT machinery of *C. elegans* cilia: two IFT dynein complexes? *PLoS ONE* **6**, e20995.
14. Li, W., Yi, P., and Ou, G. (2015). Somatic CRISPR-Cas9-induced mutations reveal roles of embryonically essential dynein chains in *Caenorhabditis elegans* cilia. *J. Cell Biol.* **208**, 683–692.
15. Pazour, G.J., Wilkerson, C.G., and Witman, G.B. (1998). A dynein light chain is essential for the retrograde particle movement of intraflagellar transport (IFT). *J. Cell Biol.* **141**, 979–992.
16. Hou, Y., Pazour, G.J., and Witman, G.B. (2004). A dynein light intermediate chain, D1bLIC, is required for retrograde intraflagellar transport. *Mol. Biol. Cell* **15**, 4382–4394.
17. Pazour, G.J., Dickert, B.L., and Witman, G.B. (1999). The DHC1b (DHC2) isoform of cytoplasmic dynein is required for flagellar assembly. *J. Cell Biol.* **144**, 473–481.
18. Porter, M.E., Bower, R., Knott, J.A., Byrd, P., and Dentler, W. (1999). Cytoplasmic dynein heavy chain 1b is required for flagellar assembly in *Chlamydomonas*. *Mol. Biol. Cell* **10**, 693–712.
19. El Hokayem, J., Huber, C., Couvé, A., Aziza, J., Baujat, G., Bouvier, R., Cavalcanti, D.P., Collins, F.A., Cordier, M.P., Delezoide, A.L., et al. (2012). NEK1 and DYNC2H1 are both involved in short rib polydactyly Majewski type but not in Beemer Langer cases. *J. Med. Genet.* **49**, 227–233.
20. Doroquez, D.B., Berciu, C., Anderson, J.R., Sengupta, P., and Nicastro, D. (2014). A high-resolution morphological and ultrastructural map of anterior sensory cilia and glia in *Caenorhabditis elegans*. *eLife* **3**, e01948.
21. Mijalkovic, J., Prevo, B., Oswald, F., Mangeol, P., and Peterman, E.J. (2017). Ensemble and single-molecule dynamics of IFT dynein in *Caenorhabditis elegans* cilia. *Nat. Commun.* **8**, 14591.
22. Ichikawa, M., Watanabe, Y., Murayama, T., and Toyoshima, Y.Y. (2011). Recombinant human cytoplasmic dynein heavy chain 1 and 2: observation of dynein-2 motor activity in vitro. *FEBS Lett.* **585**, 2419–2423.
23. Rompolas, P., Pedersen, L.B., Patel-King, R.S., and King, S.M. (2007). *Chlamydomonas* FAP133 is a dynein intermediate chain associated with the retrograde intraflagellar transport motor. *J. Cell Sci.* **120**, 3653–3665.
24. Dickinson, D.J., Ward, J.D., Reiner, D.J., and Goldstein, B. (2013). Engineering the *Caenorhabditis elegans* genome using Cas9-triggered homologous recombination. *Nat. Methods* **10**, 1028–1034.
25. Poirier, K., Lebrun, N., Broix, L., Tian, G., Saillour, Y., Boscheron, C., Parrini, E., Valence, S., Pierre, B.S., Oger, M., et al. (2013). Mutations in TUBG1, DYNC1H1, KIF5C and KIF2A cause malformations of cortical development and microcephaly. *Nat. Genet.* **45**, 639–647.
26. Schmidt, H., Zalyte, R., Urnavicius, L., and Carter, A.P. (2015). Structure of human cytoplasmic dynein-2 primed for its power stroke. *Nature* **518**, 435–438.
27. Carter, A.P., Cho, C., Jin, L., and Vale, R.D. (2011). Crystal structure of the dynein motor domain. *Science* **331**, 1159–1165.
28. Taylor, S.P., Dantas, T.J., Duran, I., Wu, S., Lachman, R.S., Nelson, S.F., Cohn, D.H., Vallee, R.B., and Krakow, D.; University of Washington Center for Mendelian Genomics Consortium (2015). Mutations in

- DYNC2LI1 disrupt cilia function and cause short rib polydactyly syndrome. *Nat. Commun.* 6, 7092.
29. Perrone, C.A., Tritschler, D., Taulman, P., Bower, R., Yoder, B.K., and Porter, M.E. (2003). A novel dynein light intermediate chain colocalizes with the retrograde motor for intraflagellar transport at sites of axoneme assembly in chlamydomonas and Mammalian cells. *Mol. Biol. Cell* 14, 2041–2056.
 30. Blisnick, T., Buisson, J., Absalon, S., Marie, A., Cayet, N., and Bastin, P. (2014). The intraflagellar transport dynein complex of trypanosomes is made of a heterodimer of dynein heavy chains and of light and intermediate chains of distinct functions. *Mol. Biol. Cell* 25, 2620–2633.
 31. Behal, R.H., Miller, M.S., Qin, H., Lucke, B.F., Jones, A., and Cole, D.G. (2012). Subunit interactions and organization of the Chlamydomonas reinhardtii intraflagellar transport complex A proteins. *J. Biol. Chem.* 287, 11689–11703.
 32. Mukhopadhyay, S., Wen, X., Chih, B., Nelson, C.D., Lane, W.S., Scales, S.J., and Jackson, P.K. (2010). TULP3 bridges the IFT-A complex and membrane phosphoinositides to promote trafficking of G protein-coupled receptors into primary cilia. *Genes Dev.* 24, 2180–2193.
 33. Niwa, S. (2016). The nephronophthisis-related gene ift-139 is required for ciliogenesis in *Caenorhabditis elegans*. *Sci. Rep.* 6, 31544.
 34. Davis, E.E., Zhang, Q., Liu, Q., Diplas, B.H., Davey, L.M., Hartley, J., Stoetzel, C., Szymanska, K., Ramaswami, G., Logan, C.V., et al.; NISC Comparative Sequencing Program (2011). TTC21B contributes both causal and modifying alleles across the ciliopathy spectrum. *Nat. Genet.* 43, 189–196.
 35. Tran, P.V., Haycraft, C.J., Besschetnova, T.Y., Turbe-Doan, A., Stottmann, R.W., Herron, B.J., Chesebro, A.L., Qiu, H., Scherz, P.J., Shah, J.V., et al. (2008). THM1 negatively modulates mouse sonic hedgehog signal transduction and affects retrograde intraflagellar transport in cilia. *Nat. Genet.* 40, 403–410.
 36. Stokman, M.F., Oud, M.M., van Binsbergen, E., Slaats, G.G., Nicolau, N., Renkema, K.Y., Nijman, I.J., Roepman, R., Giles, R.H., Arts, H.H., et al. (2016). De novo 14q24.2q24.3 microdeletion including IFT43 is associated with intellectual disability, skeletal anomalies, cardiac anomalies, and myopia. *Am. J. Med. Genet. A* 170, 1566–1569.
 37. Arts, H.H., Bongers, E.M., Mans, D.A., van Beersum, S.E., Oud, M.M., Bolat, E., Spruijt, L., Cornelissen, E.A., Schuurs-Hoeijmakers, J.H., de Leeuw, N., et al. (2011). C14ORF179 encoding IFT43 is mutated in Sensenbrenner syndrome. *J. Med. Genet.* 48, 390–395.
 38. Zhu, B., Zhu, X., Wang, L., Liang, Y., Feng, Q., and Pan, J. (2017). Functional exploration of the IFT-A complex in intraflagellar transport and ciliogenesis. *PLoS Genet.* 13, e1006627.
 39. Efimenko, E., Blacque, O.E., Ou, G., Haycraft, C.J., Yoder, B.K., Scholey, J.M., Leroux, M.R., and Swoboda, P. (2006). *Caenorhabditis elegans* DYF-2, an orthologue of human WDR19, is a component of the intraflagellar transport machinery in sensory cilia. *Mol. Biol. Cell* 17, 4801–4811.
 40. Wei, Q., Zhang, Y., Li, Y., Zhang, Q., Ling, K., and Hu, J. (2012). The BBSome controls IFT assembly and turnaround in cilia. *Nat. Cell Biol.* 14, 950–957.
 41. Kozminski, K.G., Johnson, K.A., Forscher, P., and Rosenbaum, J.L. (1993). A motility in the eukaryotic flagellum unrelated to flagellar beating. *Proc. Natl. Acad. Sci. USA* 90, 5519–5523.
 42. Jensen, V.L., Li, C., Bowie, R.V., Clarke, L., Mohan, S., Blacque, O.E., and Leroux, M.R. (2015). Formation of the transition zone by Mks5/Rgrip1L establishes a ciliary zone of exclusion (CIZE) that compartmentalises ciliary signalling proteins and controls PIP2 ciliary abundance. *EMBO J.* 34, 2537–2556.
 43. Mallik, R., Carter, B.C., Lex, S.A., King, S.J., and Gross, S.P. (2004). Cytoplasmic dynein functions as a gear in response to load. *Nature* 427, 649–652.
 44. Burghoorn, J., Dekkers, M.P., Rademakers, S., de Jong, T., Willemsen, R., and Jansen, G. (2007). Mutation of the MAP kinase DYF-5 affects docking and undocking of kinesin-2 motors and reduces their speed in the cilia of *Caenorhabditis elegans*. *Proc. Natl. Acad. Sci. USA* 104, 7157–7162.
 45. Ori-McKenney, K.M., Xu, J., Gross, S.P., and Vallee, R.B. (2010). A cytoplasmic dynein tail mutation impairs motor processivity. *Nat. Cell Biol.* 12, 1228–1234.
 46. Kardon, J.R., and Vale, R.D. (2009). Regulators of the cytoplasmic dynein motor. *Nat. Rev. Mol. Cell Biol.* 10, 854–865.
 47. Buisson, J., Chenouard, N., Lagache, T., Blisnick, T., Olivo-Marin, J.C., and Bastin, P. (2013). Intraflagellar transport proteins cycle between the flagellum and its base. *J. Cell Sci.* 126, 327–338.
 48. Engel, B.D., Ludington, W.B., and Marshall, W.F. (2009). Intraflagellar transport particle size scales inversely with flagellar length: revisiting the balance-point length control model. *J. Cell Biol.* 187, 81–89.
 49. Stepanek, L., and Pigino, G. (2016). Microtubule doublets are double-track railways for intraflagellar transport trains. *Science* 352, 721–724.
 50. Novarino, G., Akizu, N., and Gleeson, J.G. (2011). Modeling human disease in humans: the ciliopathies. *Cell* 147, 70–79.

STAR★METHODS

KEY RESOURCES TABLE

REAGENT or RESOURCE	SOURCE	IDENTIFIER
Antibodies		
Mouse anti-GFP	Roche	Cat#11814460001; RRID: AB_390913
Bacterial and Virus Strains		
BL21 (DE3)	Transgen	Cat#CD601
Chemicals, Peptides, and Recombinant Proteins		
Dil (1,1'-Diocadecyl-3,3',3'-tetramethylindocarbocyanine perchlorate)	Sigma	Cat#468495
DiO (3,3'-dioctadecyloxacarbocyanine perchlorate)	Sigma	Cat#D4292
Bovine tubulin	This paper	N/A
GST-MTBD (CHE-3)	This paper	N/A
GFP-Trap_A beads	Chromoteck	Cat#GTA20
Glutathione Sepharose 4B beads	GE HealthCare	Cat#170756
cComplete protease inhibitor	Roche	Cat#04693159001
Trypsin Gold, Mass Spectrometry Grade	Promega	Cat#V5280
Sodium fluoride	Sigma	Cat#S7920
Sodium orthovanadate	Sigma	Cat#450243
Trichloroacetic acid solution 6.1N	Sigma	Cat#T0699
Iodoacetamide	Sigma	Cat#I1149
Methylamine 40 wt. % in H ₂ O	Sigma	Cat#426466
Tris(2-carboxyethyl)phosphine hydrochloride	Sigma	Cat#75259
Formic acid	DikmaPure	Cat#50144
Levamisol hydrochloride	Sigma	Cat#31742
Critical Commercial Assays		
In-Fusion Advantage PCR Cloning Kit	Clontech	Cat#639619
Experimental Models: Organisms/Strains		
<i>C. elegans</i> : Strain SP2101: ncl-1(e1865) unc-36(e251); osm-6(p811); mnls17[Posm-6::osm-6::GFP unc-36(+)]	Caenorhabditis Genetics Center	WB Strain: SP2101; WBTransgene00001004
<i>C. elegans</i> : Strain JT11069: xbx-1(ok279)	Caenorhabditis Genetics Center	WB Strain: JT11069; WBVar00091578
<i>C. elegans</i> : Strain PR813: osm-5(p813)	Caenorhabditis Genetics Center	WB Strain; PR813; WBVar00095130
<i>C. elegans</i> : Strain CB3330: che-11(e1810)	Caenorhabditis Genetics Center	WB Strain; CB3330; WBVar00144321
<i>C. elegans</i> : Strain CB1387: daf-10(e1387)	Caenorhabditis Genetics Center	WB Strain; CB1387; WBVar00143964
<i>C. elegans</i> : Strain VC1130: ift-139(gk508)	Caenorhabditis Genetics Center	WB Strain; VC1130; WBVar00145881
<i>C. elegans</i> : Strain VC1164: ift-139(gk477)	Caenorhabditis Genetics Center	WB Strain; VC1164; WBVar00145871
<i>C. elegans</i> : Strain GOU1810: casl586(KAP-1::GFP)	This paper	N/A
<i>C. elegans</i> : Strain GOU2154: casl550(OSM-6::mCherry); him-5(e1490)	This paper	N/A
<i>C. elegans</i> : Strain GOU2356: cas443(GFP::CHE-3 knock-in)	This paper	N/A
<i>C. elegans</i> : Strain GOU2357: cas502(XBX-1::RFP::3xFlag knock-in)	This paper	N/A
<i>C. elegans</i> : Strain GOU2358: cas447(KLP-20::GFP knock-in)	This paper	N/A
<i>C. elegans</i> : Strain GOU2359: cas445(OSM-3::GFP knock-in)	This paper	N/A
<i>C. elegans</i> : Strain GOU2360: cas497(CHE-11::GFP knock-in)	This paper	N/A

(Continued on next page)

Continued

REAGENT or RESOURCE	SOURCE	IDENTIFIER
<i>C. elegans</i> : Strain GOU2361: cas498(ift-81::BFP knock-in)	This paper	N/A
<i>C. elegans</i> : Strain GOU2362: cas499(ift-74::GFP knock-in)	This paper	N/A
<i>C. elegans</i> : Strain GOU2363: cas496(GFP::CHE-3(R295C) knock-in)	This paper	N/A
<i>C. elegans</i> : Strain GOU2364: cas528(GFP::CHE-3(R1384C) knock-in)	This paper	N/A
<i>C. elegans</i> : Strain GOU2365: cas512(GFP::CHE-3(R1693C) knock-in)	This paper	N/A
<i>C. elegans</i> : Strain GOU2366: cas511(GFP::CHE-3(K2935Q) knock-in)	This paper	N/A
<i>C. elegans</i> : Strain GOU1883: casls550; che-3(cas496)	This paper	N/A
<i>C. elegans</i> : Strain GOU2221: casls550; che-3(cas512)	This paper	N/A
<i>C. elegans</i> : Strain GOU2222: casls550; che-3(cas511)	This paper	N/A
<i>C. elegans</i> : Strain GOU2367: che-3(cas332); mnls17	This paper	N/A
<i>C. elegans</i> : Strain GOU2368: cas496; casEx1675[Pdyf-1::mCherry::dyci-1; rol-6(su1006)(+)]	This paper	N/A
<i>C. elegans</i> : Strain GOU2369: cas496; casEx1676[Pxbx-1::xbx-1::mCherry; rol-6(su1006)(+)]	This paper	N/A
<i>C. elegans</i> : Strain GOU2370: cas495(GFP::CHE-3 truncation)	This paper	N/A
<i>C. elegans</i> : Strain GOU2371: cas507(GFP::CHE-3 truncation)	This paper	N/A
<i>C. elegans</i> : Strain GOU2372: cas508(GFP::CHE-3 truncation)	This paper	N/A
<i>C. elegans</i> : Strain GOU2373: cas509(GFP::CHE-3 truncation)	This paper	N/A
<i>C. elegans</i> : Strain GOU2374: cas510(GFP::CHE-3 truncation)	This paper	N/A
<i>C. elegans</i> : Strain GOU2375: cas513(GFP::CHE-3 truncation)	This paper	N/A
<i>C. elegans</i> : Strain GOU2376: cas514(GFP::CHE-3 truncation)	This paper	N/A
<i>C. elegans</i> : Strain GOU2377: cas515(GFP::CHE-3 truncation)	This paper	N/A
<i>C. elegans</i> : Strain GOU2378: cas523(GFP::CHE-3 truncation)	This paper	N/A
<i>C. elegans</i> : Strain GOU2379: cas524(GFP::CHE-3 truncation)	This paper	N/A
<i>C. elegans</i> : Strain GOU2380: cas525(GFP::CHE-3 truncation)	This paper	N/A
<i>C. elegans</i> : Strain GOU2381: cas526(GFP::CHE-3 truncation)	This paper	N/A
<i>C. elegans</i> : Strain GOU2382: cas527(GFP::CHE-3 in-frame deletion)	This paper	N/A
<i>C. elegans</i> : Strain GOU1827: xbx-1(ok279); che-3(cas443)	This paper	N/A
<i>C. elegans</i> : Strain GOU2163: che-3(cas495); xbx-1(cas502)	This paper	N/A
<i>C. elegans</i> : Strain GOU2339: daf-10(e1387); mnls17	This paper	N/A
<i>C. elegans</i> : Strain GOU2334: daf-10(e1387); xbx-1(cas502)	This paper	N/A
<i>C. elegans</i> : Strain GOU2343: daf-10(e1387); che-3(cas443)	This paper	N/A
<i>C. elegans</i> : Strain GOU2347: che-11(e1810); che-3(cas443)	This paper	N/A
<i>C. elegans</i> : Strain GOU2383: osm-5(p813); mnls17	This paper	N/A
<i>C. elegans</i> : Strain GOU2346: osm-5(p813); che-3(cas443)	This paper	N/A
<i>C. elegans</i> : Strain GOU2384: casEx1682[Pdyf-1::osm-6::mCherry; Pift-43::ift-43::gfp]	This paper	N/A
<i>C. elegans</i> : Strain GOU2385: casEx1690[Pift-139::ift-139::gfp; rol-6(su1006)(+)]	This paper	N/A
<i>C. elegans</i> : Strain GOU2167: ift-43(cas529); mnls17	This paper	N/A
<i>C. elegans</i> : Strain GOU2171: ift-43(cas530); mnls17	This paper	N/A
<i>C. elegans</i> : Strain GOU2172: ift-43(cas531); mnls17	This paper	N/A
<i>C. elegans</i> : Strain GOU2189: ift-139(gk508); mnls17	This paper	N/A
<i>C. elegans</i> : Strain GOU2191: ift-139(gk477); mnls17	This paper	N/A
<i>C. elegans</i> : Strain GOU2185: ift-43(cas530); ift-139(gk508); mnls17	This paper	N/A
<i>C. elegans</i> : Strain GOU2190: ift-43(cas531); ift-139(gk508); mnls17	This paper	N/A
<i>C. elegans</i> : Strain GOU2192: ift-43(cas530); ift-139(gk477); mnls17	This paper	N/A
<i>C. elegans</i> : Strain GOU2193: ift-43(cas531); ift-139(gk477); mnls17	This paper	N/A
<i>C. elegans</i> : Strain GOU2210: ift-43(cas530); che-3(cas443); xbx-1(cas502)	This paper	N/A

(Continued on next page)

Continued

REAGENT or RESOURCE	SOURCE	IDENTIFIER
<i>C. elegans</i> : Strain GOU2194: ift-139(gk508); che-3(cas443)	This paper	N/A
<i>C. elegans</i> : Strain GOU2196: ift-43(cas530); ift-139(gk508); che-3(cas443); xbx-1(cas502)	This paper	N/A
<i>C. elegans</i> : Strain GOU2225: ift-139(gk508); ift-74(cas499)	This paper	N/A
<i>C. elegans</i> : Strain GOU2217: ift-139(gk508); che-11(cas497)	This paper	N/A
<i>C. elegans</i> : Strain GOU2216: ift-43(cas530); che-11(cas497)	This paper	N/A
<i>C. elegans</i> : Strain GOU2215: ift-43(cas530); ift-139(gk508); che-11(cas497)	This paper	N/A
<i>C. elegans</i> : Strain GOU2430: casEx1691[Pxbx-1::xbx-1::VC155; Pift-43::ift-43::VN155; Pdyf-1::osm-6::mCherry]	This paper	N/A
<i>C. elegans</i> : Strain GOU2431: casEx1692[Pxbx-1::xbx-1::VN155; Pift-139::ift-139::VC155; Pdyf-1::osm-6::mCherry; rol-6(su1006)(+)]	This paper	N/A
<i>C. elegans</i> : Strain GOU2432: casEx1693[Pdyf-1::osm-3::VN155; Pdyf-1::klp-20::VC155; Pdyf-1::osm-6::mCherry; rol-6(su1006)(+)]	This paper	N/A
<i>C. elegans</i> : Strain GOU2461: cas443(GFP::CHE-3); casEx1713[Pdyf-1::mksr-2::mCherry; rol-6(su1006)(+)]	This paper	N/A
<i>C. elegans</i> : Strain GOU2462: GFP::CHE-3(R1384C); casEx1714[Pdyf-1::mksr-2::mCherry; rol-6(su1006)(+)]	This paper	N/A
<i>C. elegans</i> : Strain GOU2463: GFP::CHE-3(R1693C); casEx1715[Pdyf-1::mksr-2::mCherry; rol-6(su1006)(+)]	This paper	N/A
<i>C. elegans</i> : Strain GOU2464: GFP::CHE-3(R295C); casEx1716[Pdyf-1::mksr-2::mCherry; rol-6(su1006)(+)]	This paper	N/A
<i>C. elegans</i> : Strain GOU2465: GFP::CHE-3(cas495); casEx1717[Pdyf-1::mksr-2::mCherry; rol-6(su1006)(+)]	This paper	N/A
<i>C. elegans</i> : Strain GOU2466: GFP::CHE-3(cas527); casEx1718[Pdyf-1::mksr-2::mCherry; rol-6(su1006)(+)]	This paper	N/A
Oligonucleotides		
CRISPR targeting sequence (+PAM): GFP::CHE-3 KI #1: CGAGTCTGATGACATCTT(TGG)	This paper	N/A
CRISPR targeting sequence (+PAM): XBX-1::TagRFP KI #1: GAGGCTGCAGAGGCACGTG(CGG)	This paper	N/A
CRISPR targeting sequence (+PAM): OSM-3::GFP KI #1: CAATGTACACACGAATTATT(TGG)	This paper	N/A
CRISPR targeting sequence (+PAM): OSM-3::GFP KI #2: ATTTGCTGAATAGTTGCA(CGG)	This paper	N/A
CRISPR targeting sequence (+PAM): KLP-20::GFP KI #1: CAACAATTGCTCACATAAC(TGG)	This paper	N/A
CRISPR targeting sequence (+PAM): CHE-11::GFP KI #1: GTATGTGATGAAATGAGAA(TGG)	This paper	N/A
CRISPR targeting sequence (+PAM): CHE-11::GFP KI #2: GCGAAAGATAACACGTTTGT(TGG)	This paper	N/A
CRISPR targeting sequence (+PAM): IFT-74::GFP KI #1: TCAGGTGAATCTTGAAA(TGG)	This paper	N/A
CRISPR targeting sequence (+PAM): IFT-74::GFP KI #2: CTTTGCCTACAGTAGCTTTA(AGG)	This paper	N/A
CRISPR targeting sequence (+PAM): IFT-81::TagBFP KI #1: CCGCATGCAAGCTGAACCTT(TGG)	This paper	N/A
CRISPR targeting sequence (+PAM): IFT-81::TagBFP KI #2: CAAAATTGACGAGAGAGAG(AGG)	This paper	N/A
CRISPR targeting sequence (+PAM): CHE-3(R295C) KI #1: GATTGTTAACTGCTCAGACT(TGG)	This paper	N/A
CRISPR targeting sequence (+PAM): CHE-3(R295C) KI #2: GAAGTCGGGATTTCCAATT(TGG)	This paper	N/A

(Continued on next page)

Continued

REAGENT or RESOURCE	SOURCE	IDENTIFIER
CRISPR targeting sequence (+PAM): CHE-3(R1384C) KI #1: GAACGCTGTCGCTTTGC(TGG)	This paper	N/A
CRISPR targeting sequence (+PAM): CHE-3(R1693C) KI #1: GAATTTATCGCTTGATT(CGG)	This paper	N/A
CRISPR targeting sequence (+PAM): CHE-3(R2935Q) KI #1: CTTCAAAAAGTGGAGTGA(AGG)	This paper	N/A
CRISPR targeting sequence (+PAM): IFT-43 KO #1: ATACAAACAGCGTGCTGAGT(CGG)	This paper	N/A
CRISPR targeting sequence (+PAM): IFT-43 KO #2: GGTGGACGAAGAGGGTCCA(TGG)	This paper	N/A
Primers used for knock-in (KI), knockout (KO) plasmid construction and mutant screen, see Table S1	This paper	N/A
Recombinant DNA		
Plasmid: pDD162-Peft-3::Cas9+PU6::empty sgRNA	[24]	Cat#47594
Plasmid: pDD162-Peft-3::Cas9+PU6::che-3-T1 sgRNA	This paper	N/A
Plasmid: pDD162-Peft-3::Cas9+PU6::xbx-1-T1 sgRNA	This paper	N/A
Plasmid: pDD162-Peft-3::Cas9+PU6::osm-3-T1 sgRNA	This paper	N/A
Plasmid: pDD162-Peft-3::Cas9+PU6::osm-3-T2 sgRNA	This paper	N/A
Plasmid: pDD162-Peft-3::Cas9+PU6::klp-20-T1 sgRNA	This paper	N/A
Plasmid: pDD162-Peft-3::Cas9+PU6::che-11-T1 sgRNA	This paper	N/A
Plasmid: pDD162-Peft-3::Cas9+PU6::che-11-T2 sgRNA	This paper	N/A
Plasmid: pDD162-Peft-3::Cas9+PU6::ift-74-T1 sgRNA	This paper	N/A
Plasmid: pDD162-Peft-3::Cas9+PU6::ift-74-T2 sgRNA	This paper	N/A
Plasmid: pDD162-Peft-3::Cas9+PU6::ift-81-T1 sgRNA	This paper	N/A
Plasmid: pDD162-Peft-3::Cas9+PU6::ift-81-T2 sgRNA	This paper	N/A
Plasmid: pDD162-Peft-3::Cas9+PU6::che-3(R295C)-T1 sgRNA	This paper	N/A
Plasmid: pDD162-Peft-3::Cas9+PU6::che-3(R295C)-T2 sgRNA	This paper	N/A
Plasmid: pDD162-Peft-3::Cas9+PU6::che-3(R1384C)-T1 sgRNA	This paper	N/A
Plasmid: pDD162-Peft-3::Cas9+PU6::che-3(R1693C)-T1 sgRNA	This paper	N/A
Plasmid: pDD162-Peft-3::Cas9+PU6::che-3(R2935Q)-T1 sgRNA	This paper	N/A
Plasmid: pPD95.77-GFP::CHE-3 HR template	This paper	N/A
Plasmid: pPD95.77-XBX-1::TagRFP HR template	This paper	N/A
Plasmid: pPD95.77-OSM-3::GFP HR template	This paper	N/A
Plasmid: pPD95.77-KLP-20::GFP HR template	This paper	N/A
Plasmid: pPD95.77-CHE-11::GFP HR template	This paper	N/A
Plasmid: pPD95.77-IFT-74::GFP HR template	This paper	N/A
Plasmid: pPD95.77-IFT-81::TagBFP HR template	This paper	N/A
Plasmid: pPD95.77-GFP::CHE-3(R295C) HR template	This paper	N/A
Plasmid: pPD95.77-GFP::CHE-3(R1384C) HR template	This paper	N/A
Plasmid: pPD95.77-GFP::CHE-3(R1693C) HR template	This paper	N/A
Plasmid: pPD95.77-GFP::CHE-3(K2935Q) HR template	This paper	N/A
Plasmid: pDD162-Peft-3::Cas9+PU6::ift-43-T1 sgRNA	This paper	N/A
Plasmid: pDD162-Peft-3::Cas9+PU6::ift-43-T2 sgRNA	This paper	N/A
Plasmid: pDONR-Pdyf-1::mksr-2::mCherry	This paper	N/A
Plasmid: pDONR-Pdyf-1::klp-20::VC	This paper	N/A
Plasmid: pDONR-Pdyf-1::osm-3::VN	This paper	N/A
Plasmid: pGEX-6P-1-T7-GST-MTBD(CHE-3)	This paper	N/A
PCR product: Pift-43::ift-43::gfp	This paper	N/A
PCR product: Pift-139::ift-139::gfp	This paper	N/A
PCR product: Pift-43::ift-43::VN	This paper	N/A

(Continued on next page)

Continued

REAGENT or RESOURCE	SOURCE	IDENTIFIER
PCR product: Pxbx-1::xbx-1::VC	This paper	N/A
PCR product: Pift-139::ift-139::VC	This paper	N/A
PCR product: Pxbx-1::xbx-1::VN	This paper	N/A
Software and Algorithms		
μManager	Ronald Vale Lab, UCSF	https://www.micro-manager.org/
ImageJ	NIH Image	http://rsbweb.nih.gov/ij/
KymographClear & KymographDirect	[8]	http://www.nat.vu.nl/~erwinn/downloads.html
Chimera	Resource for Biocomputing, Visualization and Informatics (RBVI), UCSF	http://www.cgl.ucsf.edu/chimera/
Clustal X2.1	Conway Institute, UCD	http://www.clustal.org/
SMART	European Molecular Biology Laboratory	http://smart.embl-heidelberg.de/

CONTACT FOR REAGENT AND RESOURCE SHARING

Further information and requests for resources and reagents should be directed to and will be fulfilled by the Lead Contact, Guangshuo Ou (guangshuoou@tsinghua.edu.cn).

EXPERIMENTAL MODEL AND SUBJECT DETAILS

The wild-type *Caenorhabditis elegans* N2 was used to generate knockout, knock-in and transgenic strains. Mutant or knock-in strains were backcrossed three times to remove background mutations. Adult hermaphrodite worms were used in the dye-filling assays and live cell imaging experiments. Worms at mixed stages were collected to perform GFP immunoprecipitation and mass spectrometry. All strains were cultured on the nematode growth medium (NGM) plates seeded with *E. coli* OP50 at 20°C. All animal experiments were performed in accordance with the governmental and institutional guidelines.

METHOD DETAILS**Molecular biology**

CRISPR-Cas9 targets were inserted to the pDD162 vector (Addgene #47549) by linearizing this vector with primers listed in the Table S1. The resulting PCR products containing 15 bp overlapped double strand DNA ends were treated with DpnI digestion overnight and transformed into *E. coli*. The linearized PCR products were cyclized to generate plasmids by spontaneous recombination in bacteria. For fluorescence tag knock-in, homology recombination (HR) templates were constructed by cloning the 0.7–2.8 kb 5' and 3' homology arms into pPD95.77 plasmids using In-Fusion Advantage PCR cloning kit (Clontech, cat. no. 639621). Subsequently, fluorescence tag coding sequences were inserted into these constructs before the stop codons. Target sites in the templates were modified with synonymous mutations or removed in the non-coding region using the same strategy as introducing CRISPR targets. All tags were added to the C-terminal ends except that *che-3* was tagged with an N-terminal GFP. We generated CHE-3 point mutation knock-ins in the GFP::CHE-3 knock-in background by using the similar cloning strategies except that an additional restriction enzyme digestion site was introduced or disrupted in the HR templates, which facilitates the molecular detection of knock-in animals (Figure S2C). IFT-43::GFP and IFT-139::GFP translational reporters were constructed by SOEing PCR of *ift-43* and *ift-139a* genomic sequences (1250 bp promoter plus coding for *ift-43* and 726 bp promoter plus coding for *ift-139a*) with GFP::unc-54 3'UTR fragments. Bimolecular fluorescence complementation (BiFC) constructs of *ift-43*, *ift-139a* and *xbx-1* were generated by SOEing PCR of genomic sequences under the expression of their endogenous promoters (2.3 kb promoter plus coding for *xbx-1*) with the Venus N-terminal fragment (VN) or C-terminal fragment (VC) plus unc-54 3' UTR. BiFC constructs for *osm-3* and *klp-20* were generated by cloning VN/VC into the pDONR vectors containing 445 bp *dyf-1* promoter, *osm-3* or *klp-20* cDNA and unc-54 3' UTR using In-Fusion Advantage PCR cloning kit.

Genome editing

CRISPR-Cas9 constructs and HR templates were purified with AxyPrep Plasmid Purification Miniprep Kit (Axygen, #AP-MN-P-250) and PureLink Quick PCR purification Kit (Invitrogen, cat. no. K310001) and co-injected into gonads of young adult worms with

rol-6(1006) and *Podr-1::dsRed* selection markers. Marker-positive F1 progenies were singled and screened by PCR-amplifying a genomic fragment covering a portion of the 3' homology arm up to beyond the 5' homology arm region (Figure 1A). Only knock-in animals can be amplified to produce a predominant DNA band. To screen point mutation knock-in animals, an additional restriction digestion step was performed before gel electrophoresis. *ift-43* mutants were generated by CRISPR-Cas9-mediated germline knockout with two sgRNA targets that introduced large deletions, which were identified by PCR amplification and gel electrophoresis. All mutations were verified by sequencing the entire genes to guarantee that no other mutations were inserted on the target genes.

Microinjection and transgenesis

Extra-chromosomal transgenic lines of IFT-43::GFP were obtained by co-injecting the *Pift-43::ift-43::gfp* PCR products with *Pdyf-1::osm-6::mCherry* plasmid. IFT-139::GFP transgenic lines were obtained by co-injecting the *Pift-139::ift-139::gfp* PCR products with *rol-6(su1006)* plasmid. *Pift-43::ift-43::VN* + *Pxbx-1::xbx-1::VC*, *Pxbx-1::xbx-1::VN* + *Pift-139::ift-139::VC* or *Pdyf-1::osm-3::VN* + *Pdyf-1::klp-20::VC* pairs were co-injected with *Pdyf-1::osm-6::mCherry* and *rol-6(su1006)* plasmids. Microinjection was performed using the wild-type strain N2 except that GFP::CHE-3 knock-in animals were used to generate point mutation knock-ins. Concentration of each DNA construct for microinjection was ~50 ng/μl. For all knock-in lines, extra-chromosomal transgenes were discarded before sequencing and phenotypic analysis. For expression analyses of IFT-43::GFP, IFT-139::GFP and BiFC pairs, at least two or three independent transgenic lines were examined.

Dye-filling assay

Young adult worms were randomly collected into 100~200 μL M9 solution and mixed with equal volume dyes (Dil 1,1'-dioctadecyl-3,3,3',3'-tetramethylindo-carbocyanine perchlorate, or DiO 3,3'-dioctadecyloxacarbocyanine perchlorate, Sigma) at working concentration (20 μg/ml), followed by incubation at room temperature in dark for 30-60 min. Worms were transferred to seeded NGM plates and examined for dye uptake one hour later using compound microscopes. At least 100 worms of each strain were examined in two independent assays. No blinding test was performed.

Live cell imaging

Young adult *C. elegans* hermaphrodites were anesthetized with 0.1 mmol/L levamisole in M9 buffer, mounted on 3% agar pads, and maintained at room temperature. Our regular imaging system includes an Axio Observer Z1 microscope (Carl Zeiss) equipped with a 100×, 1.46 NA objective lens, an EMCCD camera (iXon+ DU-897D-C00-#BV-500; Andor Technology), and the 405 nm, 488 nm and 568 nm lines of a Sapphire CW CDRH USB Laser System (Coherent) with a spinning disk confocal scan head (CSU-X1 Spinning Disk Unit; Yokogawa Electric Corporation). Our high-resolution live imaging system includes an Olympus IX83 microscope equipped with a 150x, 1.45 NA objective lens, a Neo 5.5 sCMOS Camera (DC-152Q-C00-Fl; Andor Technology) and the same spinning disk confocal modules as mentioned above. Time-lapse images were acquired by μManager (<https://www.micro-manager.org>) at an exposure time of 200 ms in Figure 1 and of 100 ms in Figure 2 and 3.

Image processing and analysis

We used ImageJ software (<http://rsbweb.nih.gov/ij/>) to process images, generate kymographs and collect the original data for quantifications of cilium length and velocity. We used a ciliary marker OSM-6::GFP to measure the length of the cilia in *che-3* null mutant, *ift-43* and *ift-139* mutant animals. For animals carrying ciliopathy-related point mutations of *che-3*, we measured the length of the cilia using the distribution of GFP::CHE-3 fluorescence. Considering that GFP::CHE-3 and the ciliary marker OSM-6::mCherry showed the identical distribution pattern in *che-3* mutant alleles (Figures S4A, S4E and S4F), both markers can faithfully reflect the length of the cilia. To ensure the quality of images used for velocity calculation, movies only in stable focal planes that cover the whole cilium structures were used to generate kymographs. For detailed analysis of IFT speeds in Figures 2 and 3, Fourier filtered and separated anterograde and retrograde kymographs were generated with the KymographClear toolset plugin in ImageJ (<http://www.nat.vu.nl/~erwipn/downloads.html>) by manually drawing lines along cilia at the width of five pixels. Complete tracks of individual IFT particles along the whole cilium length were manually selected and carefully drawn in the KymographClear toolset. IFT velocities at different positions along cilia were automatically extracted in the KymographDirect software (<http://www.nat.vu.nl/~erwipn/downloads.html>), classified into groups at the distance of every 0.5 μm along cilia and further quantified to generate the velocity curves in Figure 2B. For a rough calculation of velocities at different ciliary subregions, IFT velocities were further grouped into three classes at the distance of every 3 μm and quantified in Figures 2C–2E. Particles that could not be tracked along the full length of cilia or were not clearly separate were not used for quantifications. In Figure 3F, distribution of IFT velocities were fit by Gaussian distribution.

Mass spectrometry

Unsynchronized transgenic or knock-in strains raised on 80~100 90-mm NGM plates were collected and washed for three times with M9 buffer. Lysates were made from 1~2 mL packed worms in lysis buffer (25 mM Tris-HCl, pH 7.4, 150 mM NaCl, 1% NP-40, 10% glycerol, 1x cocktail of protease inhibitors from Roche (Complete, EDTA free), 40 mM NaF, 5 mM Na₃VO₄) and 3~4 mL of 0.5-mm diameter glass beads using FastPrep-24 (MP Biomedicals). Proteins were immunoprecipitated with GFP-Trap A beads (Chromoteck) and eluted with 300 μL 0.1 M glycine-HCl, pH 2.5 into 15 μL 1.5 M Tris-HCl pH 8.8, followed by precipitation with 100 μL trichloroacetic acid and re-dissolution in 60 μL 8 M urea, 100 mM Tris-HCl, pH 8.5. Samples were treated with 5 mM TCEP for reduction,

10 mM iodoacetamide for alkylation and then diluted fourfold with 100 mM Tris-HCl 8.5. The proteins were digested with 0.2 µg trypsin at 37°C overnight after the addition of 1 mM CaCl₂ and 20 mM methylamine and the resultant peptides were desalted with ZipTip pipette tips (Merck Millipore). For liquid chromatography-tandem mass spectrometry analysis, peptides were separated by a flow rate of 0.250 µL/min using an EASY-nLCII integrated nano-HPLC system (Proxeon, Odense, Denmark), which was directly interfaced to a Thermo Scientific Q Exactive mass spectrometer. The analytical column was a fused-silica capillary column (75 µm in internal diameter, 150 mm in length; Upchurch) packed with C-18 resin (300 Å, 5 µm; Varian). Mobile phase A consisted of 0.1% formic acid, and mobile phase B consisted of 100% acetonitrile and 0.1% formic acid. The Q Exactive mass spectrometer was operated in data-dependent acquisition mode using Xcalibur 2.1.2 software, and there was a single full-scan mass spectrum in the orbitrap (400–1,800 m/z, 60,000 resolution) followed by ten data-dependent tandem mass spectrometry scans at 27% normalized collision energy (HCD). The tandem mass spectrometry spectra were searched against a *C. elegans* proteome database using Proteome Discoverer (version PD1.4; Thermo Fisher Scientific). The protein components in the list in Figure 5 were reproducibly identified from multiple biological repeats: KAP-1::GFP (n = 2), KLP-20::GFP (n = 2), OSM-6::GFP (n = 2), IFT-74::GFP (n = 3) and CHE-11::GFP (n = 2).

Structure analysis, bioinformatics and biochemistry

Structures of mouse DYNC1H1 MTBD with tubulin dimer (PDB: 3J1T, 3J1U) and human DYNC2H1 motor domain (PDB: 4RH7) were viewed and processed in Chimera (<http://www.cgl.ucsf.edu/chimera/>). DNA sequence alignment was performed using Clustal X2.1 (<http://www.clustal.org/>). Protein sequences were obtained from Wormbase (<http://www.wormbase.org/>) or National Center for Biotechnology Information (www.ncbi.nlm.nih.gov/). Conserved domains in dynein-2, IFT43 and IFT139 were identified by SMART (simple modular architecture research tool) (<http://smart.embl-heidelberg.de/>) or CDD (NCBI's conserved domain database) online tools. WT and K2935Q mutant MTBDs (22:19, CHE-3^{2857–3021}, complete sequence shown in Figure S2B) were fused to GST tag (pGEX-6P-1), expressed in *E. coli* BL21 (DE3), and purified with glutathione Sepharose 4B beads (GE Healthcare, lot# 10223936). Bovine tubulins were polymerized in vitro at 37°C in BRB80 buffer. WT and K2935Q MTBD at different concentrations (see Figure S3 legend) were incubated with polymerized MT in parallel for 1 hr in BRB25 buffer at room temperature and centrifuged at 10,0000 g for 30 min. Supernatants and pellets were separated and loaded on 10% SDS-PAGE gel. Protein amounts in the supernatants and pellets were quantified in ImageJ.

QUANTIFICATION AND STATISTICAL ANALYSIS

Quantification was represented by the mean value ± standard deviation for each group. Two-tailed Student's t test analysis was used to examine all significant differences between groups as indicated in the figure legends. N represents the number of animals used for cilium length quantification (Figures 3D and 6C), the number of IFT particles used for velocity quantification (Figures 1E, 3F, 5F and 6G), the number of velocities along cilium subdomains (Figures 2B–2E, 3G and 3H) or the number of kymographs used for IFT frequency quantification (Figures 3I and 6F). Significance was determined when the p value is lower than 0.05. The variance is similar between the groups that are being statistically compared unless it is mentioned in the text.

Supplemental Information

Dynein-Driven Retrograde Intraflagellar Transport

Is Triphasic in *C. elegans* Sensory Cilia

Peishan Yi, Wen-Jun Li, Meng-Qiu Dong, and Guangshuo Ou

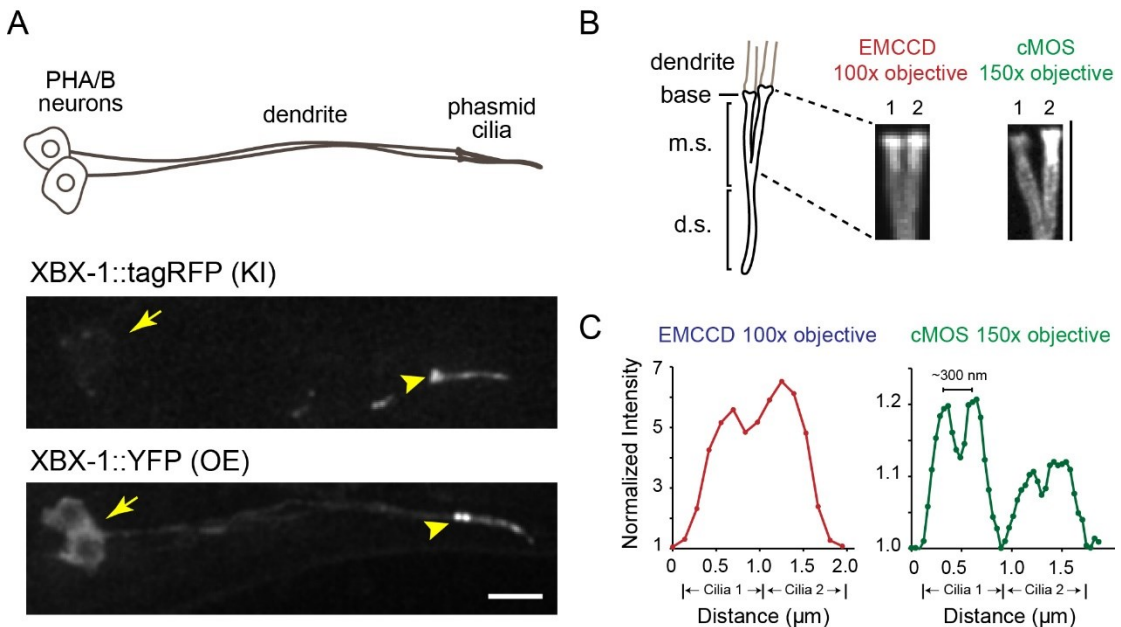


Figure S1. Improved fluorescence imaging of *C. elegans* sensory cilia. Related to Figure 1 and 2.

(A) Comparison of fluorescence signals in XBX-1 overexpression (OE) and knock-in (KI) lines. Fluorescence in the cell body and dendrite of the KI strain is weaker than that in the overexpression line. Arrows indicate the cell bodies of PHA/B neurons. Arrowheads indicate the ciliary bases of phasmid cilia. Scale bar: 5 μm .

(B-C) Imaging of the endogenous dynein-2 heavy chain (GFP::CHE-3) movement with an EMCCD camera and a 100x objective (red) or a cMOS camera and a 150x objective (green). A pair of phasmid cilia (numbered as 1 and 2) extend from the PHA or PHB dendritic endings and each consists of the ciliary base, middle segment (m.s.) and distal segments (d.s.). A stack containing 200 time-lapse frames of the middle segments were projected at maximal intensity into a single plane to show the overall location of multiple particles (also see Movie S1). Note with improved image acquisition (right), two major tracks appear distinguishable, which were confirmed by plot of normalized intensity across the middle segments in (C). The distance between the two tracks is $\sim 300 \text{ nm}$. Scale bar: 5 μm .

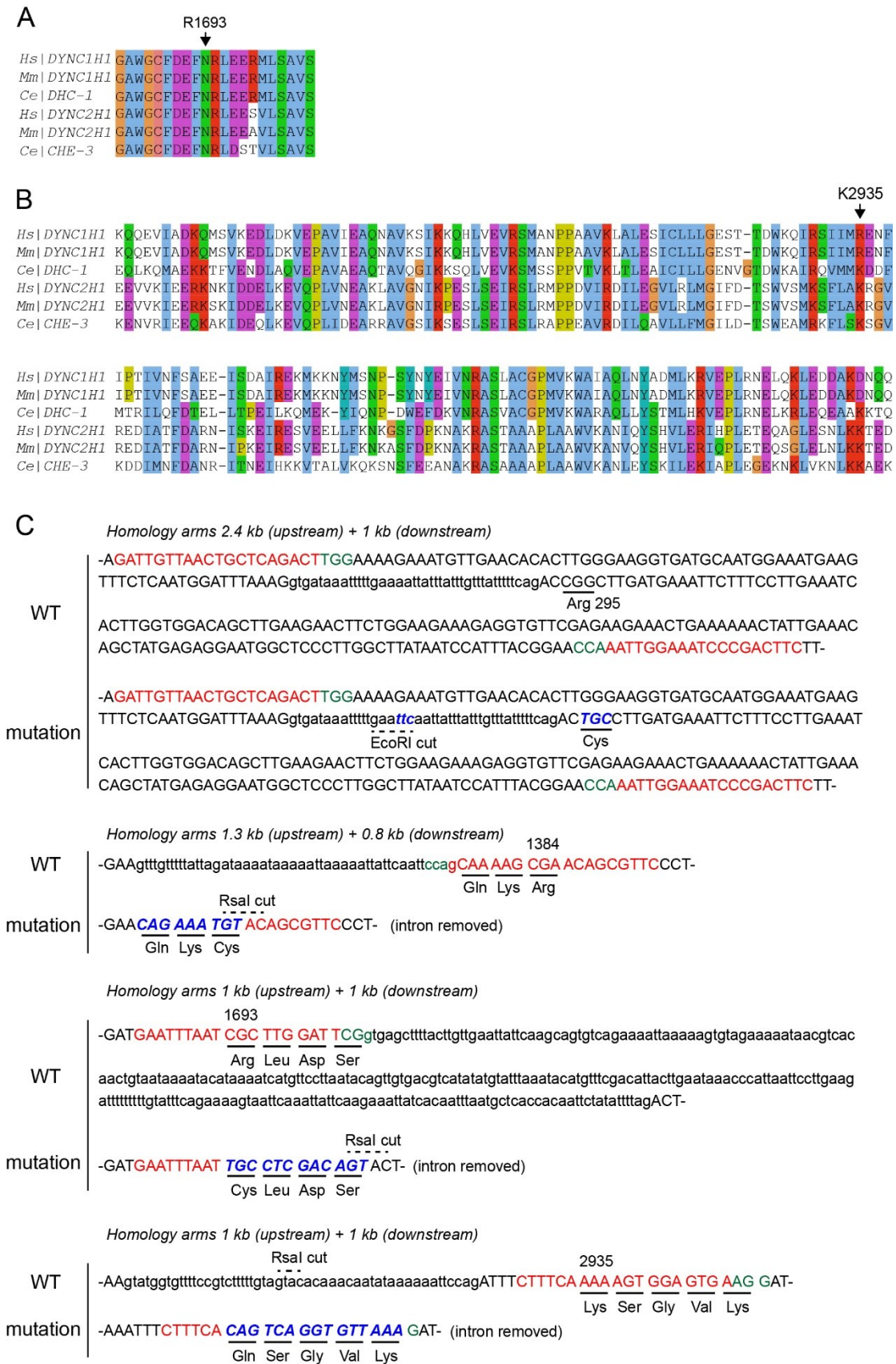


Figure S2. Alignments of dynein sequences and construction of homology recombination templates with disease-related mutations. Related to Figure 3.

- (A) Alignment of cytoplasmic dynein-1 and dynein-2 sequences from human (*Hs*, DYNC1H1 NCBI: NP_001367.2; DYNC2H1 NCBI: NP_001073932.1), mouse (*Mm*, DYNC1H1 NCBI: NP_084514.2; DYNC2H1 NCBI: NP_084127.2), and *C. elegans* (*Ce*, DHC-1 NCBI: NP_491363.1; CHE-3 NCBI: NP_492221.2). Arrow indicates the R1693 residue in CHE-3.
- (B) Alignment of microtubule binding domain (MTBD, CHE-3²⁸⁵⁷⁻³⁰²¹) of cytoplasmic dynein-1 and dynein-2. Arrow indicates K2935 in CHE-3.
- (C) Construction of homology recombination templates to generate disease-related point mutation knock-in strains in the *gfp::che-3* background. CRISPR targets and PAM motifs in WT genomes are colored in red and green, respectively. Mutations in templates are colored in blue. A restriction enzyme cutting site was introduced or disrupted as labelled for each target. If necessary, introns were modified or removed.

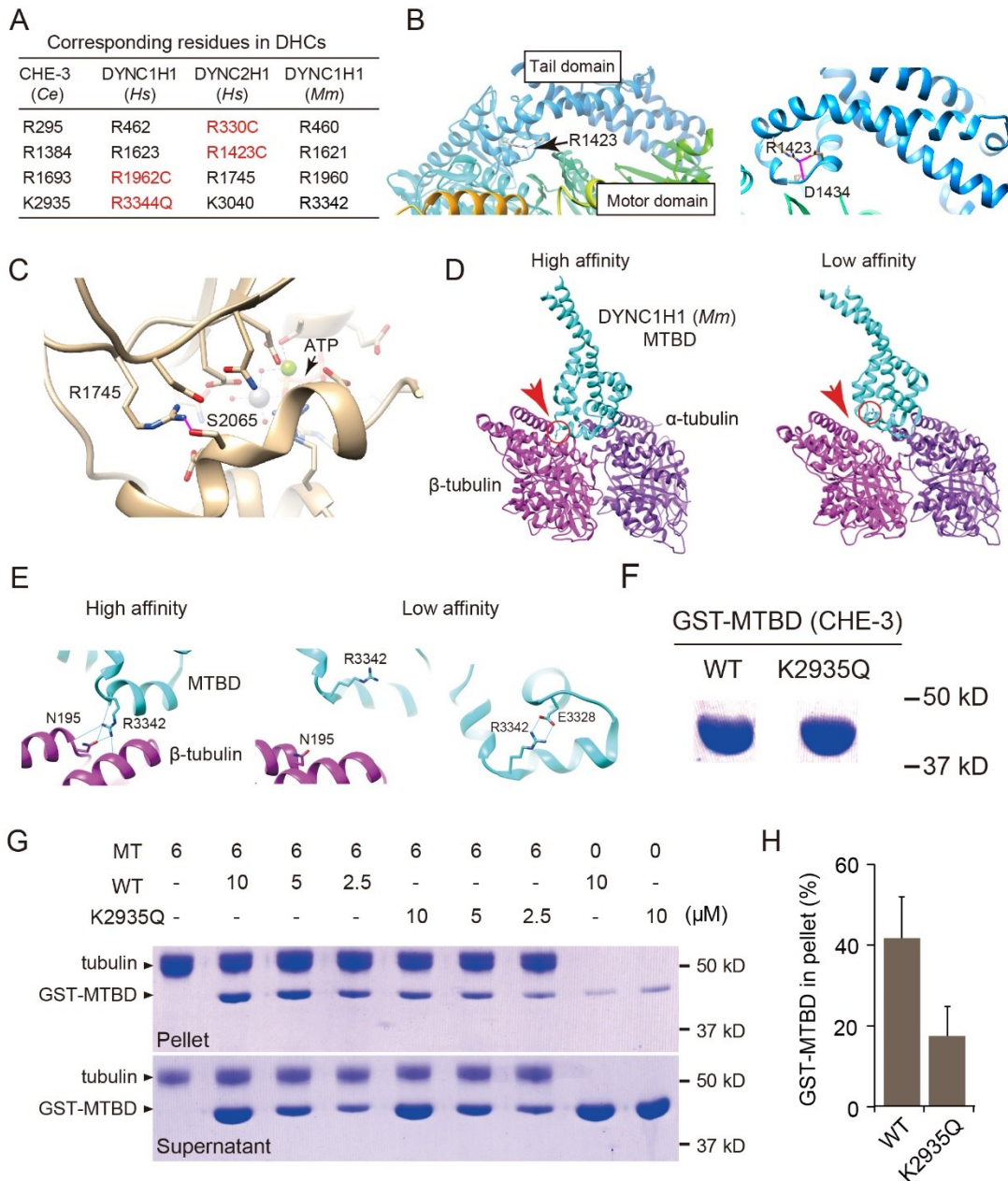


Figure S3. Structural and biochemical analysis of disease-related mutations. Related to Figure 3.

- (A) Corresponding residues in *C. elegans* (*Ce*) CHE-3, human (*Hs*) cytoplasmic dynein-1 (DYNC1H1) and dynein-2 (DYNC2H1) heavy chains and mouse (*Mm*) cytoplasmic dynein-1 (DYNC1H1) heavy chain. Disease-related mutations are colored in red.
- (B) Location of R1423 residue in human DYNC2H1 structure (PDB: 4RH7). Putative hydrogen bonds between R1423 and D1434 are indicated by pink lines.
- (C) Location of R1745 residue in human DYNC2H1 AAA1 domain (PDB: 4RH7). Arrow indicates ATP. A putative hydrogen bond between R1745 and S2065 is indicated by a

pink line.

(D) Structures of mouse DYNC1H1 MTBD domain (cyan) binding with α -tubulin: β -tubulin dimer with high (left, PDB: 3J1T) or low (right, PDB: 3J1U) binding affinity. Red arrows indicate contact surface between β -tubulin and R3342 residue.

(E) Positioning of R3342 in mouse DYNC1H1 MTBD structures co-crystallized with tubulin dimer with high (PDB: 3J1T, above) or low (PDB: 3J1U, below) affinity. Putative hydrogen bonds are indicated by cyan lines. Note that R3342 side chain is released from the MTBD: β -tubulin interface in the low affinity state and forms internal hydrogen bonds with E3382.

(F) Purification of the recombinant WT and K2935Q mutant GST-MTBD of CHE-3. The MTBD corresponds to CHE-3²⁸⁵⁷⁻³⁰²¹ and its complete sequence is shown in Figure S2B.

(G) Microtubule pelleting assay. Polymerized microtubules (6 μ M) were co-sedimented with WT and GST-MTBD^{K2935Q} at different concentrations. Microtubule binding affinity was saturated at about 5 μ M with WT GST-MTBD.

(H) Quantification of WT GST-MTBD or GST-MTBD^{K2935Q} fractions at the concentration of 5 μ M co-sedimented with MT in the pelleting assays (mean \pm s.d.). Three independent assays were performed at this concentration.

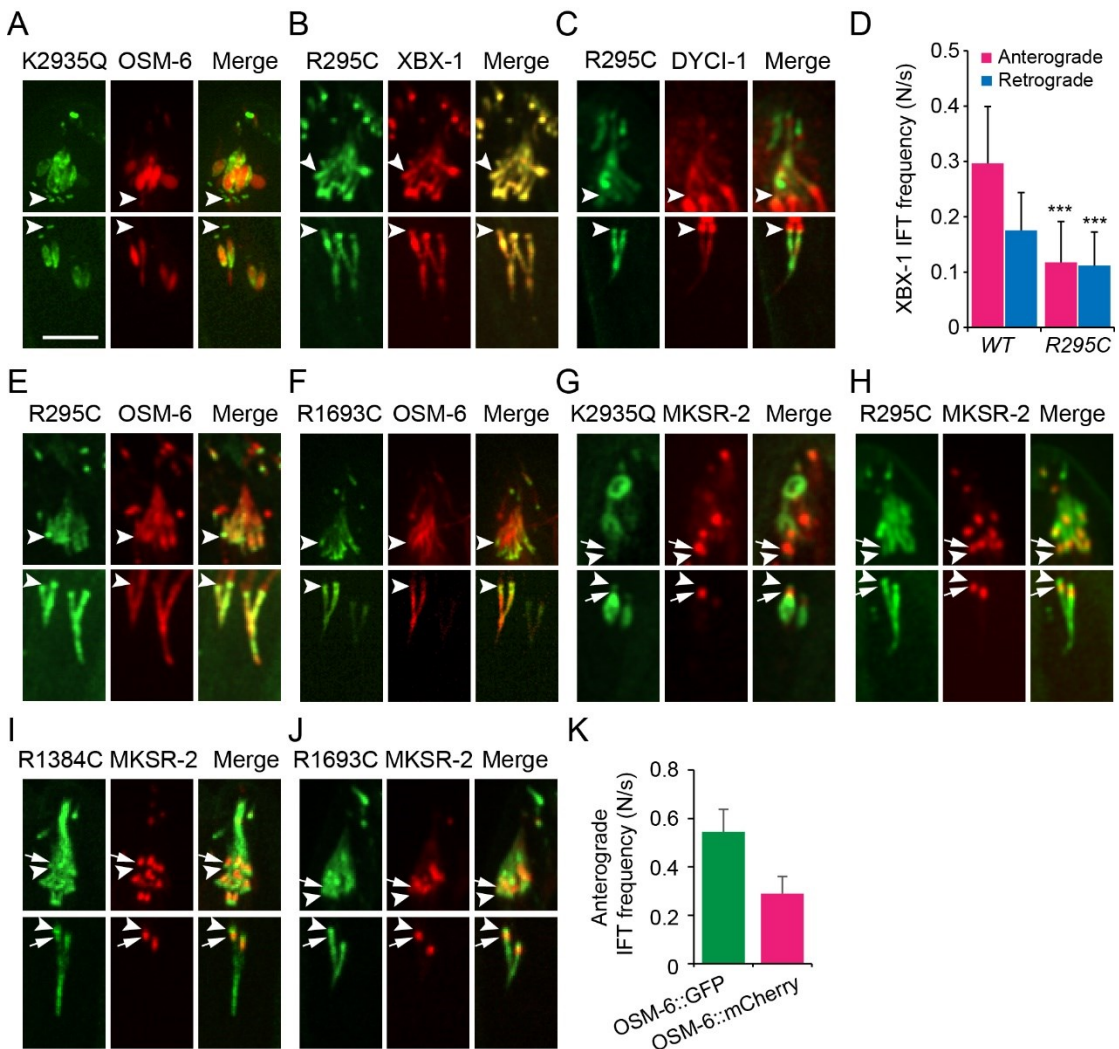


Figure S4. Colocalization of the dynein accessory chains, IFT particles and transition zone protein with GFP::CHE-3 that contains disease-related mutations. Related to Figure 3.

- (A) IFT52/OSM-6::mCherry accumulates in the GFP::CHE-3(K2935Q) mutant background. Arrowheads indicate the ciliary bases. Scale bar: 5 μ m (the same below).
- (B-C) LIC/XBX-1::mCherry and IC/DYCI-1::mCherry are colocalized with GFP::CHE-3(R295C).
- (D) Both anterograde (magenta) and retrograde (green) IFT frequencies of XBX-1::TagRFP are reduced in dynein-2 animals carrying R295C mutation (mean \pm s.d., WT n=15, R295C n=27). ***, $p < 0.001$.
- (E-F) IFT-52/OSM-6::mCherry does not accumulate in the GFP::CHE-3(R295C) and GFP::CHE-3(R1693C) background.

(G-J) Transition zone (labelled by MKSR-2::mCherry) appears grossly normal in the disease-related mutants. Arrowheads indicate the ciliary base, and arrows indicate the transition zone.

(K) Anterograde IFT frequency of OSM-6::mCherry is ~2 fold smaller than that of OSM-6::GFP (mean \pm s.d.).

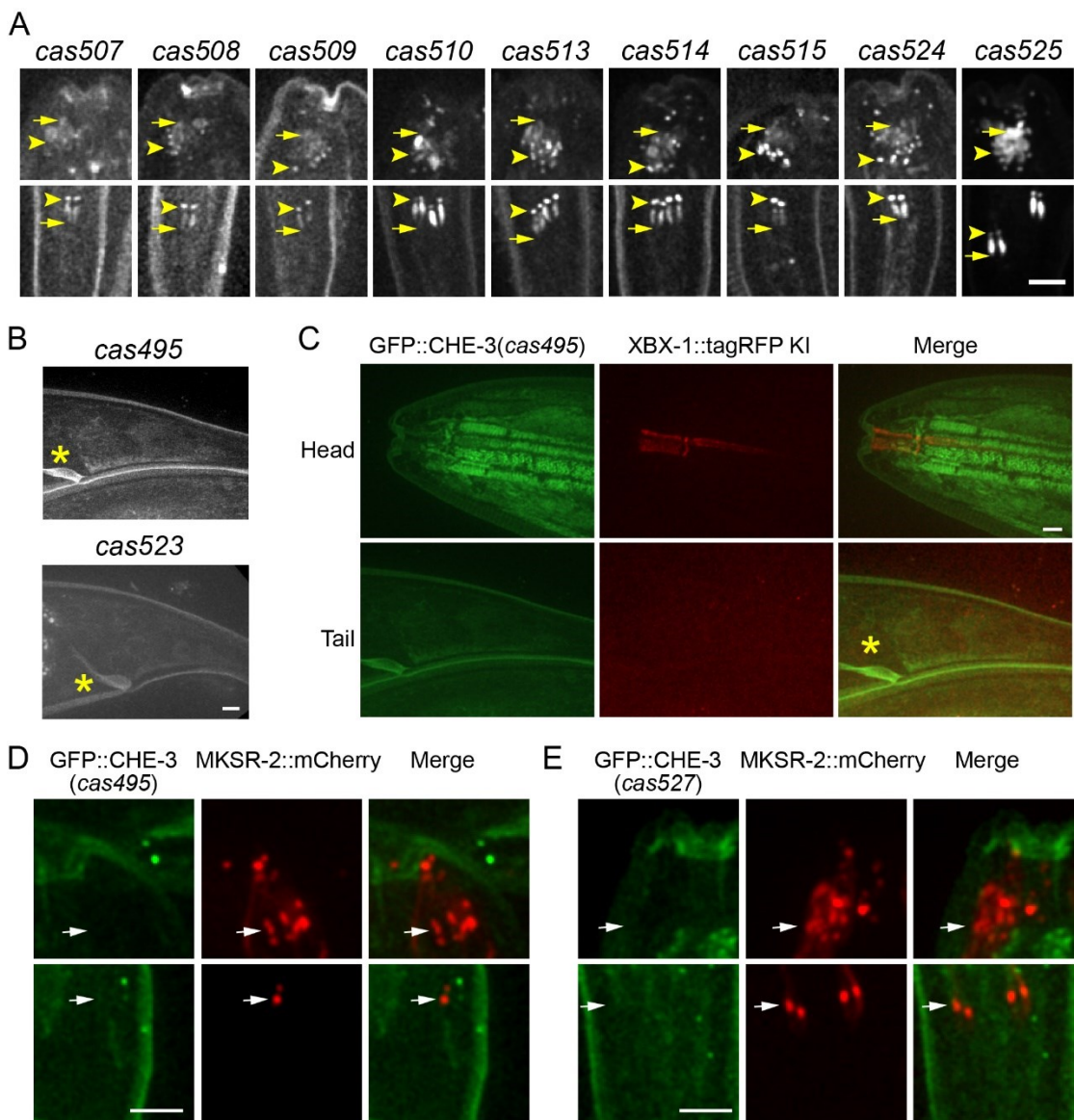


Figure S5. Ciliary localization of the truncated GFP::CHE-3. Related to Figure 4.

- (A) Truncated GFP::CHE-3 lacking the motor domain but containing a full tail domain enters the short and bulged cilia (also see Figures 4B and 4C). Arrowheads indicate the ciliary base and transition zone. Arrows indicate junctions between the middle and distal segments. Scale bar: 5 μ m.
- (B) Truncated GFP::CHE-3 lacking the motor domain and part of the tail domain is invisible in cell body or cilia. Asterisks indicate the *C. elegans* anuses. Scale bar: 5 μ m.
- (C) XBX-1::TagRFP is visible in WT background (see also Figure S1A), but is undetectable in the cilia or cell body of the putative *che-3* null mutant animals. The asterisks indicate the *C. elegans* anus. Scale bar: 5 μ m.
- (D-E) Transition zone marker MKSR-2::mCherry (arrow) marks the putative location of

cilia in the truncated GFP::CHE-3 mutants lacking the motor domain and part of the tail domain. Scale bar: 5 μ m.

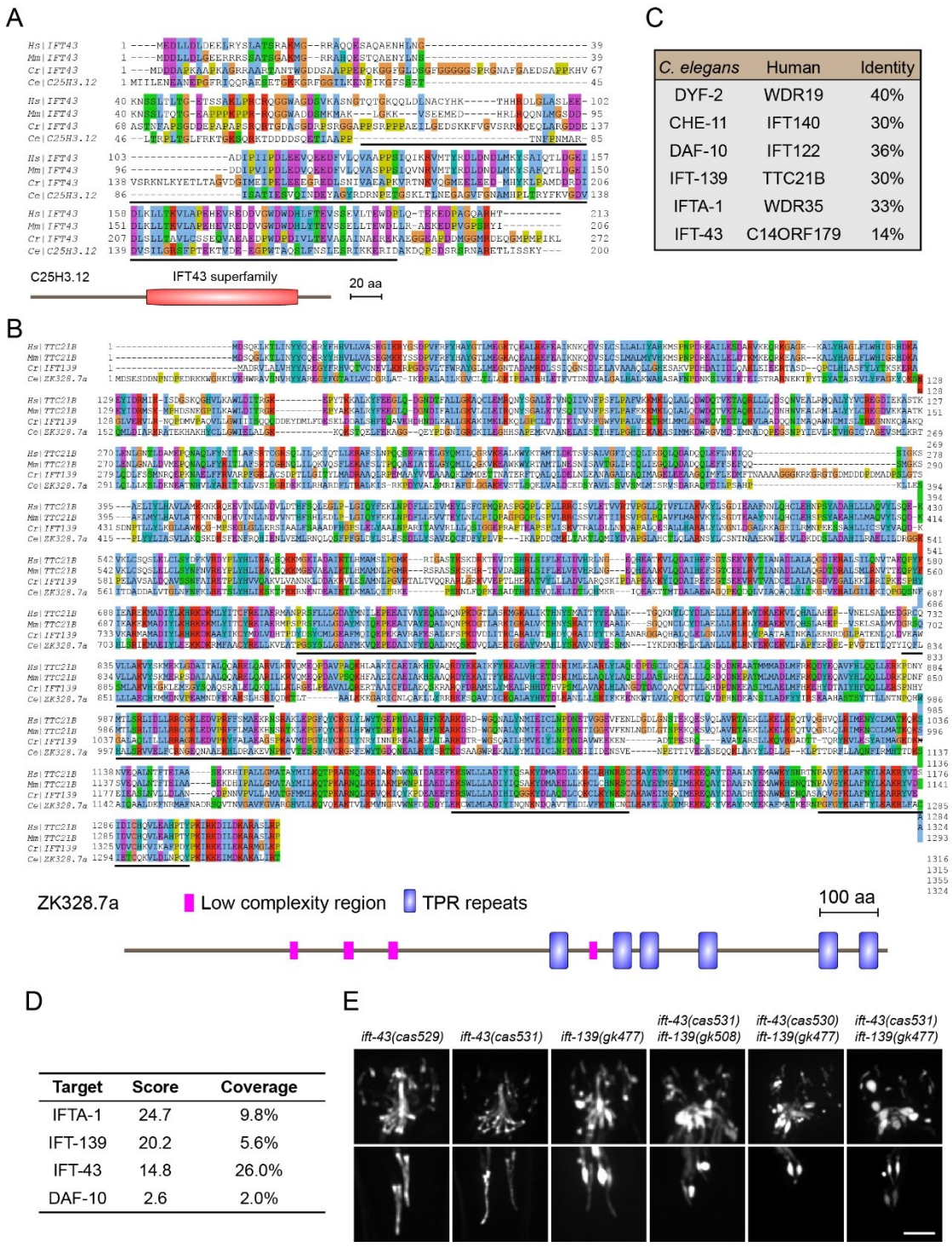


Figure S6. Sequence alignments of IFT-43 and IFT-139 homologs and their mutant phenotypes in *C. elegans*. Related to Figure 5.

(A) Alignment of human (NCBI: NP_443105.2, *Hs*), mouse (NCBI: NP_001186772.1, *Mm*), *Chlamydomonas* (NCBI: ABU93234.1, *Cr*) IFT43 and *C. elegans* C25H3.12 (NCBI: CCD65040.1, *Ce*). The putative IFT43 superfamily domain was underlined and shown in the protein structure (lower). This domain is less conserved in *C. elegans* C25H3.12.

- (B) Alignment of human TTC21B (NCBI: AAH55424.1), mouse TTC21B (NCBI: Q0HA38.1), *Chlamydomonas* IFT139 (NCBI: ABU95018.1) and *C. elegans* ZK328.7a (NCBI: CCD70957.1). The tetratricopeptide repeats (TPRs) in ZK328.7a were underlined and shown in the protein structure (lower).
- (C) Identify of IFT-A subunits between *C. elegans* and Human homologs.
- (D) Mass spectrometry result of C25H3.12::GFP.
- (E) Cilium morphology visualized with IFT52/OSM-6::GFP in *ift-43*, *ift-139* single and double mutants. Scale bar: 5 μ m.